



Fault tracing in multistage gearbox systems based on an improved transfer path analysis method

Penghong Lu^a, Cai Li^a, Gang Chen^b, Gang Chen^{a,*}

^a Shien-Ming Wu School of Intelligent Engineering, South China University Of Technology, Guangzhou, 511442, China

^b School of Naval Architecture Ocean and Energy Power Engineering, Wuhan University of Technology, Wuhan, 430070, China

ARTICLE INFO

Keywords:

Improved transfer path

MWI

Fault tracing

Gearbox fault diagnosis

Fault characteristic enhancement

ABSTRACT

This study has developed a novel structural dynamics decoupling method based on TPA. This approach effectively facilitates fault diagnosis and tracing in multistage gearbox systems. Initially, the research explores the relationship between the transfer function of systems with rigid link decoupling and the coupled system's frequency response function. Compared with Huangfu et al. (2023), the signal measurement points are reduced. The MWI (Yu et al., 2023) is employed to solve the inverse problem of bearing force identification. Subsequently, the decoupled frequency response and bearing forces are multiplied to calculate the path contribution, determining the dominant fault transfer path and thereby facilitating fault tracing in gearboxes. The effectiveness of this method is validated through numerical simulations and experimental studies, with fault characteristic enhancement exceeding 200%. To evaluate the method's universality and robustness, experiments on diverse gearbox systems under varying conditions show enhanced fault characteristics across three fault types, confirming its generalizability.

1. Introduction

Transfer Path Analysis (TPA) is extensively utilized for analyzing and addressing vibration and noise issues in complex mechanical systems, with extensive experimental validation confirming its effectiveness [1–3]. TPA is capable of identifying and quantifying excitation sources, analyzing the energy transfer pathways to the target point, and accurately assessing and ranking the contributions of different transfer paths [4,5]. By controlling and improving these paths, vibration and noise can be maintained within predetermined targets, facilitating fault tracing and diagnosis in mechanical systems. Following the “source-path-receiver” model’s inception, TPA has evolved significantly. The TPA family primarily encompasses traditional TPA [6,7], Operational TPA (OPA) [8–10], OPAX [11], Component-based TPA [12,13], and the Global Direct Transfer Rate method [14,15], also known as advanced TPA. Despite traditional TPA’s high accuracy, methodological maturity, and information richness, its complex testing process and significant assembly errors lead to suboptimal analysis efficiency [16]. To improve the analytical efficiency of traditional TPA, rapid advancements have been made in dynamic decoupling methods leveraging dynamic substructure technology [17]. Dynamic substructure technology is crucial for the evaluation of dynamic behavior in mechanically complex structures that are not amenable to holistic analysis. These techniques enable the construction of dynamic models for extensive,

intricate systems through the integration of dynamic models of their respective subsystems and substructures [18]. To alleviate the workload in acquiring substructural dynamic characteristics, researchers have developed various methods, broadly classified into in-situ decoupling methods [19–21] and standard decoupling methods [22–24]. In-situ decoupling methods typically entail decoupling substructures on a smooth surface and representing them as a series of interconnected links, while standard decoupling methods necessitate substructures possessing predetermined, a priori characteristics.

Gearboxes serve as vital components in various mechanical systems, ensuring the smooth transfer of power. However, their complex nature makes diagnosing faults a challenging endeavor. In recent years, the application of TPA methodologies has emerged as a promising approach in tracing gearbox faults. By dissecting the intricate pathways through which vibration energy propagates, TPA facilitates the identification and isolation of fault signals, thereby enhancing diagnostic precision and fault tracing. When applying TPA to fault signal identification, the standard decoupling methods (also known as physics-based methods) assumes that vibration signals obtained from gearbox housing are not affected by the transfer path, namely transfer path effects should be nullified [25–27]. These physics-based methods aimed at revealing fault-specific characteristics concealed within the signal transfer process. In these methods, Frequency Response Function (FRF) and

* Corresponding author.

E-mail address: gangchen@scut.edu.cn (G. Chen).

interface forces serve as the preferred metrics in characterizing transfer paths. While the decoupling of the FRF from gearbox housing, particularly in complex gear systems, poses a formidable challenge due to the complex structure and working conditions. Additionally, the time-intensive nature of testing and the potential alteration of assembly conditions during physical decoupling present further complications. As a result, in-situ decoupling methods (also known as visual decoupling methods) for gear transfer systems have attracted increasing research interest [19,28]. In 2018, Wang et al. [29] developed a novel TPA method that relies on in-situ measurement of frequency response functions, systematically examining the interaction between coupled and decoupled transfer functions, specifically in the context of automotive body vibrations. In 2023, Huangfu et al. [30] introduced a specialized in-situ TPA technique for gear systems, designed to facilitate effective fault tracking and mitigate the contaminating effects of gear system transfer paths. However, their approach in prevailing studies models the connection between active and passive parts as a parallel combination of springs and dampers, a simplification that may overlook certain physical characteristics [17,28,31]. Moreover, the in-situ measurement process for decoupling gearbox system frequency responses requires a substantial number of measurement points to construct decoupled transfer functions using transfer rate matrices. This undoubtedly increase some measurement difficulties related to determination of transfer functions of components. This also necessitates extensive measurement equipment, escalating both time and financial expenditures, and possibly increasing the risk of measurement errors.

In the pursuit of extracting comprehensive fault information through transfer path analysis theory, it is critical to accurately identify the bearing interface forces in gearbox systems. Present research methodologies primarily encompass three approaches: direct measurement [32], the parameter load method [11], and the inverse identification method [33]. Direct measurement in gear systems is challenging due to the necessity of integrating force sensors at the bearing locations, a process often fraught with practical difficulties. The parameter load method, reliant on vibration signals from active parts, encounters obstacles in gear rotor systems, where installing accelerometers is problematic due to their rotational nature. The inverse identification method, more suitable for gear systems, eliminates the need for additional measurement instruments. In Ref. [30], the Tikhonov regularization technique is employed to acquire reasonable solutions by introducing a regularization parameter. It may provide better identification accuracy for large matrix dimensions (experimental results show that the limit is around 100) or extremely severe ill-conditioned problems. However, this approach has its limitations, it is easy to cause systematic deviation introduced by the regular term. Yu et al. [34] have proposed a methodology for identifying bearing forces in gear systems, focusing on bearing forces as opposed to housing responses for gear fault detection. This method addresses the ill-posed inverse problem inherent in positive matrix formulation using the Maximally Weighted Iteration (MWI). This property ensures that the time-domain waveforms of bearing dynamic forces can be correctly reconstructed through the identified spectra, without being affected by the systematic deviation introduced by the regular term.

For further alleviate some measurement difficulties related to determination of transfer functions of components, also to accurately identify the bearing force, we propose a method for virtual decoupling frequency response functions, combined with Maximally Weighted Iteration(MWI) [34,35] to identify bearing forces, and an enhanced transfer path analysis method for fault tracing in multistage gearbox systems. This method proposed herein supplements existing gearbox fault tracing techniques, providing a solid foundation for fault tracing and diagnosis based on the generalized virtual decoupling approach. Additionally, path contributions constructed using transfer functions from virtual decoupling and bearing forces from the MWI facilitate fault information tracing. A physically interpretable signal decomposition method is also introduced to amplify fault characteristics. This study presents several valuable conclusions that contribute to both the theory and practice of fault diagnosis in multistage parallel gear systems:

- A novel structural dynamics decoupling method has been developed, eliminating the need for physical disassembly of complex gearbox systems. This significantly simplifies the maintenance process, reduces the likelihood of assembly errors, and minimizes measurement complexities, thus providing a more efficient and reliable diagnostic tool for industrial applications.
- The application of MWI offers clear advantages over traditional Tikhonov regularization, especially in terms of solution stability and consistency. This provides a more robust and reliable approach for analyzing fault signatures, ensuring high accuracy in real-world scenarios.
- Experimental results demonstrate that fault indicators for various fault types were amplified by over 200%, allowing for more sensitive detection of early-stage faults. This substantial amplification not only enhances diagnostic precision but also extends the system's fault detection capabilities.
- The method has shown strong generalization and robustness across different gearbox systems and operational conditions. The significantly enhanced fault features for multiple fault types under various experimental conditions confirm that the proposed method is versatile and effective, providing a reliable diagnostic solution for diverse industrial settings.

2. Theoretical fundamental

In Transfer Path Analysis (TPA) technology, there are two different types of methods. The first type involves methods using load response, and the second type is based on output signal measurements. This paper focuses only on the methods based on load response and studies the “Source-Path-Receiver” model within the TPA framework, assuming that the link between the active part (Source) and the passive part (Receiver) allows only translational vibrations. In a gear system, the gear rotor system, bearing interface, and the housing are referred to as the active part, interface part, and passive part, respectively (as shown in Fig. 1). The meshing positions between gear pairs are treated as two excitation sources, with the gearbox housing acting as the receiver, and the bearing forces as the contact forces between the active and passive parts. The essence of the TPA method is to obtain the decoupled frequency response and bearing forces between the bearing interface and the gearbox housing. In literature [30], Huangfu and others successfully conducted fault diagnosis of gearbox systems using a transfer path analysis method based on in-situ measurements. However, this method views the linkage between the active and passive parts as a parallel connection of springs and dampers, overlooking some physical characteristics. The paper then introduces a new and improved virtual decoupling method, known as the Link-Preserving Decoupling Method, for fault tracing and diagnosis in gearbox systems. This method derives two types of decoupled frequency responses corresponding to different measurement points (i.e., the $H_{c,mp}$ and $H_{c,pp}$ based methods shown in Fig. 2), both effectively facilitating fault tracing and diagnosis. Compared to literature [30], the second decoupled frequency responses reduces the number of measurement points, significantly lowers the computational load, and saves time costs.

For gearbox systems, modeling the transfer function under working conditions as \mathbf{H} and the dynamic forces of bearings as \mathbf{F} allows for a more effective representation of the gear's fault state. The specific process of fault tracing and diagnosis in gearboxes proposed in this paper can be briefly described as follows: First, considering the mass effect of elastic links between the active and passive parts of the gearbox, a decoupled transfer path analysis is conducted to construct the decoupled transfer function matrix \mathbf{H} . Then, using the MWI, the inverse problem composed of the test signal x and \mathbf{H} under different conditions is solved to estimate the different transfer paths \mathbf{F} in the actual gearbox system. Next, the estimated \mathbf{F} under fault conditions is multiplied by the corresponding decoupled transfer function to obtain the contributions of different transfer paths. By comparing these

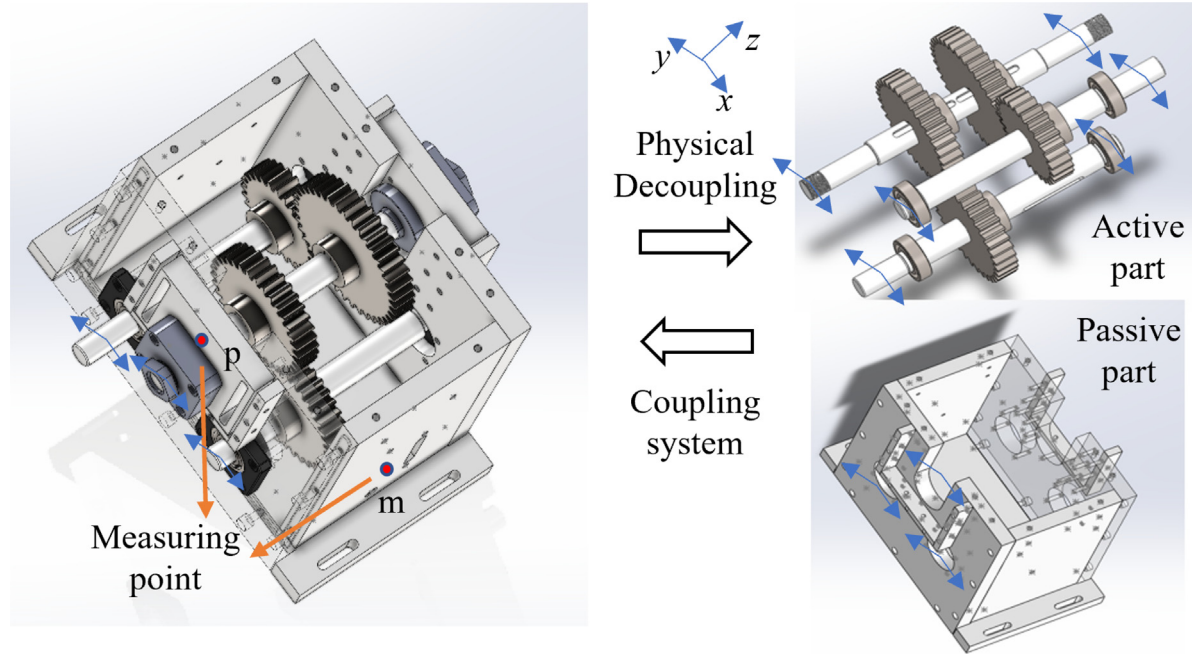


Fig. 1. The gearbox decoupling system.

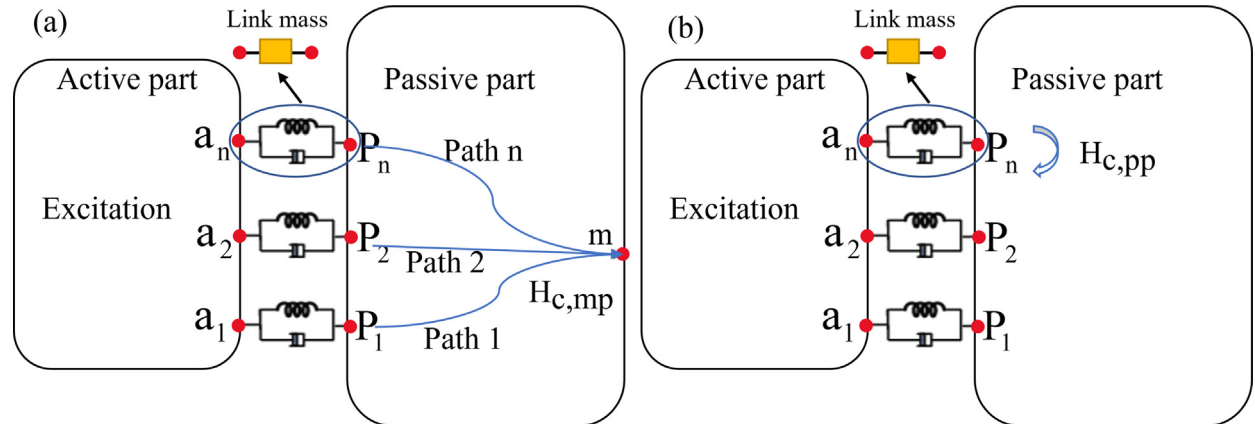


Fig. 2. Gearbox transfer path model. The symbol a denotes the interface nodes located on the side of the rotor, while the p represents the interface nodes located on the side of the house. The symbol m represents the measurement point on the side of the house. (a) The transfer function $H_{c,mp}$ is measured at the house 'm'; (b) The transfer function $H_{c,pp}$ is measured at the house 'p'.

contributions, the dominant transfer paths of the fault frequency is determined, achieving gearbox fault tracing. Finally, based on the above research, a signal decomposition method is proposed to enhance fault characteristics, effectively realizing fault tracing and diagnosis. This process is illustrated in Fig. 3. In subsequent research, we will discuss the details of this method in depth.

2.1. The lumped parameter model for a coupled system

Use a simple lumped parameter model to explain the coupling of elastic links to active and passive subsystems. Fig. 2 shows an example of a lumped parameter system, where the primary and secondary subsystems are connected by springs and dampers. This model represents the most compact form of a lumped parameter system, with active and passive sides being interlinked. Each linkage is considered a parallel

connection of a spring and a damper. The motion equation for a finite-dimensional, multi-degree-of-freedom linear structure can be written as:

$$\mathbf{M}\ddot{\mathbf{s}} + \mathbf{C}\dot{\mathbf{s}} + \mathbf{K}\mathbf{s} = \mathbf{f} \quad (1)$$

where \mathbf{M} , \mathbf{C} , and \mathbf{K} matrices respectively represent the mass, damping, and stiffness of the system. Specific experimental parameters are shown in Table 1. \mathbf{f} and \mathbf{s} represent the generalized coordinate vector and the generalized force vector. The generalized coordinates of the lumped parameter model are:

$$\mathbf{q} = [x_1, \theta_1, x_2, \theta_2, x_3, \theta_3, x_4, x_5, x_6, x_7] \quad (2)$$

where x_i and θ_i respectively represent the linear displacement and angular displacement of the i th part of the lumped parameter model. The structure of the above matrices is as follows:

$$\mathbf{M}^{coup} = \text{diag}(m_1, J_1, m_2, J_2, m_3, J_3, m_4, m_5, m_6, m_7) \quad (3)$$

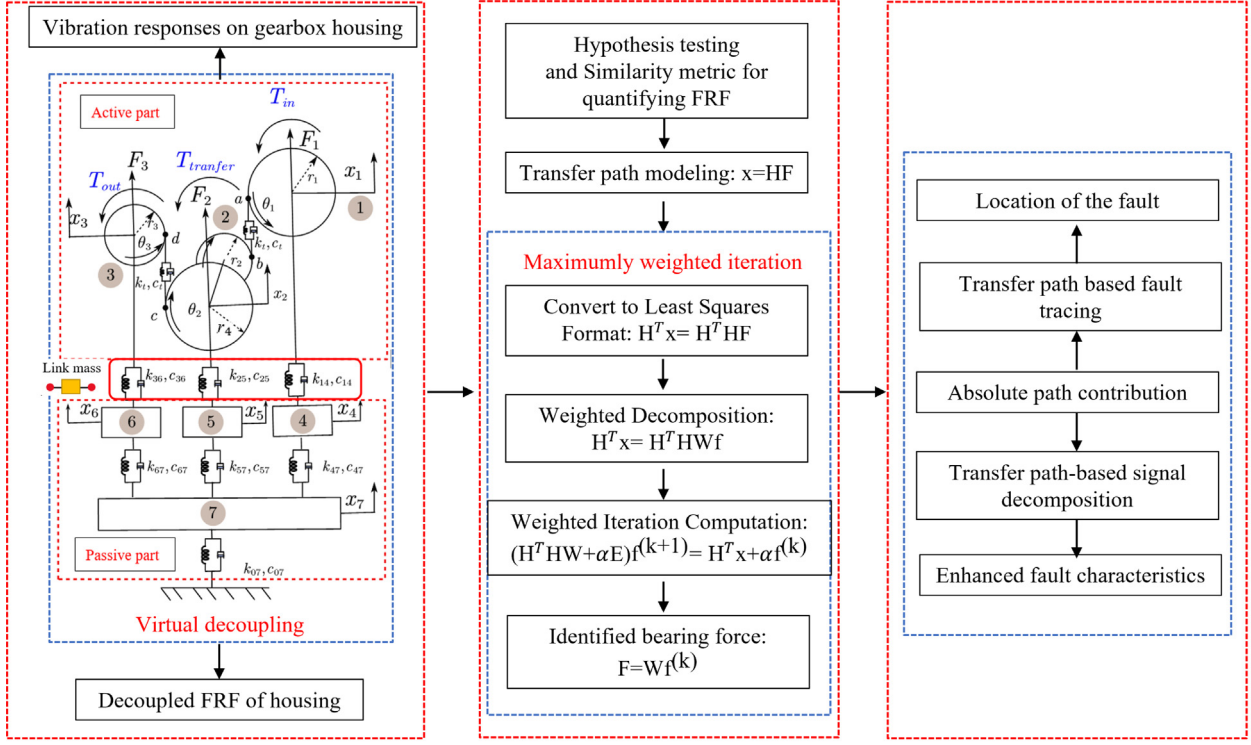


Fig. 3. The flow chart of the proposed method.

where m_i and J_i stand for the mass and moment of inertia of the i th part of the lumped model, respectively.

$$\mathbf{K}^{coup} = [K_1^{coup}, K_2^{coup}]$$

where

$$K_1^{coup} = \begin{bmatrix} k_{14} + k_1(t) & r_{b1}k_1(t) & -k_1(t) & r_{b2}k_1(t) & 0 \\ r_{b1}k_1(t) & r_{b1}^2k_1(t) & -r_{b1}k_1(t) & r_{b1}r_{b2}k_1(t) & 0 \\ -k_1(t) & r_{b1}k_1(t) & k_1(t) + k_2(t) & -r_{b2}k_1(t) + r_{b3}k_2(t) & -k_2(t) \\ r_{b2}k(t) & r_{b1}r_{b2}k_1(t) & -r_{b1}k_2(t) + r_{b3}k_2(t) & r_{b2}^2k_1(t) + r_{b3}^2k_2(t) & -r_{b3}k_2(t) \\ 0 & 0 & -k_2(t) & -r_{b3}k_2(t) & k_2(t) \\ 0 & 0 & r_{b4}k_2(t) & r_{b3}r_{b4}k_2(t) & -r_{b4}k_2(t) \\ -k_{14} & 0 & 0 & 0 & 0 \\ 0 & 0 & -k_{25} & 0 & 0 \\ 0 & 0 & 0 & 0 & -k_{36} \\ 0 & 0 & 0 & 0 & 0 \end{bmatrix}$$

$$K_2^{coup} = \begin{bmatrix} 0 & -k_{14} & 0 & 0 & 0 \\ 0 & 0 & 0 & 0 & 0 \\ r_{b4}k_2(t) & 0 & -k_{25} & 0 & 0 \\ r_{b3}r_{b4}k_2(t) & 0 & 0 & 0 & 0 \\ -r_{b4}k_2(t) & 0 & 0 & -k_{36} & 0 \\ r_{b4}^2k_2(t) & 0 & 0 & 0 & 0 \\ 0 & k_{14} + k_{47} & 0 & 0 & -k_{47} \\ 0 & 0 & k_{25} + k_{57} & 0 & -k_{57} \\ 0 & 0 & 0 & k_{36} + k_{67} & -k_{67} \\ 0 & -k_{47} & -k_{57} & -k_{67} & k_{47} + k_{57} + k_{67} + k_{07} \end{bmatrix}$$

where k_{ij} is the stiffness between part i and j . r_{bi} stand for base radius of i th gear. $k_i(t)$ represents the time-variable meshing stiffness of gear pair i .

$$\mathbf{C}^{coup} = [C_1^{coup}, C_2^{coup}] \quad (5)$$

where

$$C_1^{coup} =$$

$$(4) \quad \begin{bmatrix} c_{14} + c_1(t) & r_{b1}c_1(t) & -c_1(t) & r_{b2}c_1(t) & 0 \\ r_{b1}c_1(t) & r_{b1}^2c_1(t) & -r_{b1}c_1(t) & r_{b1}r_{b2}c_1(t) & 0 \\ -c_1(t) & r_{b1}c_1(t) & c_1(t) + c_2(t) & -r_{b2}c_1(t) + r_{b3}c_2(t) & -c_2(t) \\ r_{b2}c(t) & r_{b1}r_{b2}c_1(t) & -r_{b1}c_2(t) + r_{b3}c_2(t) & r_{b2}^2c_1(t) + r_{b3}^2c_2(t) & -r_{b3}c_2(t) \\ 0 & 0 & -c_2(t) & -r_{b3}c_2(t) & c_2(t) \\ 0 & 0 & r_{b4}c_2(t) & r_{b3}r_{b4}c_2(t) & -r_{b4}c_2(t) \\ -c_{14} & 0 & 0 & 0 & 0 \\ 0 & 0 & -c_{25} & 0 & 0 \\ 0 & 0 & 0 & 0 & -c_{36} \\ 0 & 0 & 0 & 0 & 0 \end{bmatrix}$$

$$C_2^{coup} = \begin{bmatrix} 0 & -c_{14} & 0 & 0 & 0 \\ 0 & 0 & 0 & 0 & 0 \\ r_{b4}c_2(t) & 0 & -c_{25} & 0 & 0 \\ r_{b3}r_{b4}c_2(t) & 0 & 0 & 0 & 0 \\ -r_{b4}c_2(t) & 0 & 0 & -c_{36} & 0 \\ r_{b4}^2c_2(t) & 0 & 0 & 0 & 0 \\ 0 & c_{14} + c_{47} & 0 & 0 & -c_{47} \\ 0 & 0 & c_{25} + c_{57} & 0 & -c_{57} \\ 0 & 0 & 0 & c_{36} + c_{67} & -c_{67} \\ 0 & -c_{47} & -c_{57} & -c_{67} & c_{47} + c_{57} + c_{67} + c_{07} \end{bmatrix}$$

where c_{ij} is the stiffness between part i and j . $c_i(t)$ represents the time-variable meshing stiffness of gear pair i .

The theoretical FRF of the overall system (coupled system) can be expressed as:

$$\mathbf{H}^{coup} = \omega^2 (-\omega^2 \mathbf{M}^{coup} + j\omega \mathbf{C}^{coup} + \mathbf{K}^{coup})^{-1} \quad (6)$$

where \mathbf{C}^{coup} and \mathbf{K}^{coup} are the time-averaged damping and stiffness matrices of the coupled system, respectively. When analyzing the modal characteristics of gear systems, a widely accepted strategy is to average the damping and stiffness matrices over time [30].

However, as mentioned earlier, there is interest in the transfer function within the passive subsystem. Given the lumped parameter model, this subsystem's transfer function can be easily derived:

$$\mathbf{H}^{Decoupl} = \omega^2 (-\omega^2 \mathbf{M}^{Decoupl} + j\omega \mathbf{C}^{Decoupl} + \mathbf{K}^{Decoupl})^{-1} \quad (7)$$

For the passive part, the mentioned matrices have the following structure:

$$\mathbf{M}^{Decoup} = \text{diag}(m_4, m_5, m_6, m_7)$$

$$\mathbf{K}^{Decoup} = \begin{bmatrix} k_{47} & 0 & 0 & -k_{47} \\ 0 & k_{57} & 0 & -k_{57} \\ 0 & 0 & k_{67} & -k_{67} \\ -k_{47} & -k_{57} & -k_{67} & k_{47} + k_{57} + k_{67} + k_{07} \end{bmatrix};$$

$$\mathbf{C}^{Decoup} = \begin{bmatrix} c_{47} & 0 & 0 & -c_{47} \\ 0 & c_{57} & 0 & -c_{57} \\ 0 & 0 & c_{67} & -c_{67} \\ -c_{47} & -c_{57} & -c_{67} & c_{47} + c_{57} + c_{67} + c_{07} \end{bmatrix}$$

The following section will discuss how to obtain the frequency response function of the passive system using the decoupling method.

2.2. The decoupling method

In real-life applications, obtaining the decoupled transfer function of the passive part of the system is challenging. The ultimate goal of the link-preserving decoupling method is to use the frequency response of the coupled system to predict the frequency response of the passive part. This section aims to improve the accuracy of the decoupled transfer function estimation when the link quality is effective. We apply the decoupled transfer functions method based on in-situ transfer functions [29] for analysis, and the main contents of this method are introduced below. A typical mechanical system, as shown in Fig. 3, has its active and passive parts connected in parallel by springs and dampers, considering only translational vibrations. The relationship between external force \mathbf{F} and system response \mathbf{X} is as follows:

$$\mathbf{X}(\omega) = \mathbf{H}(\omega)\mathbf{F}(\omega) \quad \text{or} \quad \mathbf{F}(\omega) = \mathbf{Z}(\omega)\mathbf{X}(\omega) \quad (8)$$

where $\mathbf{H}(\omega)$ is the system transfer function matrix, and $\mathbf{Z}(\omega)$ is the system dynamic stiffness matrix. From here on the dependency on frequency is omitted for clarity.

When focussing on the link connection points, Splitting \mathbf{Z} in a first part containing the systems $\mathbf{Z}_{d,pp}$ and $\mathbf{Z}_{d,aa}$, and a second part containing the link parameters, and the results can be found in literature [28] as follows.

$$\begin{bmatrix} * & * & 0 & 0 \\ * & \mathbf{Z}_{d,pp} & 0 & 0 \\ 0 & 0 & \mathbf{Z}_{d,aa} & * \\ 0 & 0 & * & * \end{bmatrix} \mathbf{H} + \begin{bmatrix} 0 & 0 & 0 & 0 \\ 0 & \mathbf{L}' & -\mathbf{L}' & 0 \\ 0 & -\mathbf{L}' & \mathbf{L}' & 0 \\ 0 & 0 & 0 & 0 \end{bmatrix} \mathbf{H} = \mathbf{I} \quad (9)$$

In this expression $\mathbf{Z}^{-1} = \mathbf{H}$. The matrix consists of a measurable part and an unmeasurable part, and the unmeasurable part is represented by *. For presentational reasons a more symbolic expression is introduced:

$$\left(\mathbf{Z}_1 + \begin{bmatrix} 0 & 0 & 0 \\ 0 & \mathbf{L} & 0 \\ 0 & 0 & 0 \end{bmatrix} \right) \mathbf{H} = \mathbf{I} \quad (10)$$

with

$$\mathbf{Z}_1 = \begin{bmatrix} * & * & 0 & 0 \\ * & \mathbf{Z}_{d,pp} & 0 & 0 \\ 0 & 0 & \mathbf{Z}_{d,aa} & * \\ 0 & 0 & * & * \end{bmatrix} \quad \text{and} \quad \mathbf{L} = \begin{bmatrix} \mathbf{L}' & -\mathbf{L}' \\ -\mathbf{L}' & \mathbf{L}' \end{bmatrix} \quad (11)$$

Pre-multiplying Eq. (10) by \mathbf{H}_1 yields:

$$\mathbf{H}_1 \left(\mathbf{Z}_1 + \begin{bmatrix} 0 & 0 & 0 \\ 0 & \mathbf{L} & 0 \\ 0 & 0 & 0 \end{bmatrix} \right) \mathbf{H} = \mathbf{H}_1 \quad (12)$$

where: $\mathbf{H}_1 = \mathbf{Z}_1^{-1}$.

Sorting can obtain:

$$\begin{aligned} \mathbf{H}_1 &= \begin{bmatrix} * & * & * \\ * & \hat{\mathbf{H}} & * \\ * & * & * \end{bmatrix} \begin{bmatrix} \mathbf{I} & 0 & 0 \\ * & \mathbf{I} - \mathbf{L}\hat{\mathbf{H}} & * \\ 0 & 0 & \mathbf{I} \end{bmatrix}^{-1} = \begin{bmatrix} * & * & * \\ * & \hat{\mathbf{H}} & * \\ * & * & * \end{bmatrix} \\ &\times \begin{bmatrix} \mathbf{I} & 0 & 0 \\ * & (\mathbf{I} - \mathbf{L}\hat{\mathbf{H}})^{-1} & * \\ 0 & 0 & \mathbf{I} \end{bmatrix} \end{aligned} \quad (13)$$

Taking into consideration the block structure of \mathbf{Z}_1 , the expression can be written as follows:

$$\mathbf{Z}_1 = \begin{bmatrix} * & * & 0 & 0 \\ * & \mathbf{Z}_{d,pp} & 0 & 0 \\ 0 & 0 & \mathbf{Z}_{d,aa} & * \\ 0 & 0 & * & * \end{bmatrix} = \hat{\mathbf{H}}(\mathbf{I} - \mathbf{L}\hat{\mathbf{H}})^{-1} \quad (14)$$

It can clearly be observed that the middle section containing $\mathbf{H}_{d,pp}$ and $\mathbf{H}_{d,aa}$ results in

$$\begin{bmatrix} \mathbf{H}_{d,pp} & 0 \\ 0 & \mathbf{H}_{d,aa} \end{bmatrix} = \hat{\mathbf{H}}(\mathbf{I} - \mathbf{L}\hat{\mathbf{H}})^{-1} \quad (15)$$

Taking into considering the structure of \mathbf{L} :

$$\mathbf{L} = \begin{bmatrix} \mathbf{L}' & -\mathbf{L}' \\ -\mathbf{L}' & \mathbf{L}' \end{bmatrix} = \begin{bmatrix} \mathbf{L}' & 0 \\ 0 & \mathbf{L}' \end{bmatrix} \begin{bmatrix} \mathbf{I} & -\mathbf{I} \\ -\mathbf{I} & \mathbf{I} \end{bmatrix} \quad (16)$$

Eq. (14) is modified as follows:

$$\begin{bmatrix} \mathbf{H}_{d,pp} & 0 \\ 0 & \mathbf{H}_{d,aa} \end{bmatrix} = \begin{bmatrix} \hat{\mathbf{H}}_{pp} & \hat{\mathbf{H}}_{pa} \\ \hat{\mathbf{H}}_{ap} & \hat{\mathbf{H}}_{aa} \end{bmatrix} \left(\begin{bmatrix} \mathbf{I} & 0 \\ 0 & \mathbf{I} \end{bmatrix} - \begin{bmatrix} \mathbf{L}' & 0 \\ 0 & \mathbf{L}' \end{bmatrix} \begin{bmatrix} \mathbf{I} & -\mathbf{I} \\ -\mathbf{I} & \mathbf{I} \end{bmatrix} \right)^{-1} \times \begin{bmatrix} \hat{\mathbf{H}}_{pp} & \hat{\mathbf{H}}_{pa} \\ \hat{\mathbf{H}}_{ap} & \hat{\mathbf{H}}_{aa} \end{bmatrix} \quad (17)$$

Executing the matrix product between the brackets yields:

$$\begin{aligned} \begin{bmatrix} \mathbf{H}_{d,pp} & 0 \\ 0 & \mathbf{H}_{d,aa} \end{bmatrix} &- \begin{bmatrix} \mathbf{H}_{d,pp} \mathbf{L}' & 0 \\ 0 & \mathbf{H}_{d,aa} \mathbf{L}' \end{bmatrix} \\ &= \begin{bmatrix} \hat{\mathbf{H}}_{pp} - \hat{\mathbf{H}}_{ap} & \hat{\mathbf{H}}_{pa} - \hat{\mathbf{H}}_{aa} \\ \hat{\mathbf{H}}_{ap} - \hat{\mathbf{H}}_{pp} & \hat{\mathbf{H}}_{aa} - \hat{\mathbf{H}}_{pa} \end{bmatrix} \begin{bmatrix} \hat{\mathbf{H}}_{pp} & \hat{\mathbf{H}}_{pa} \\ \hat{\mathbf{H}}_{ap} & \hat{\mathbf{H}}_{aa} \end{bmatrix} \end{aligned} \quad (18)$$

The first row of Eq. (17), gives rise to the following expression:

$$[\mathbf{H}_{d,pp} \quad 0] - \mathbf{H}_{d,pp} \mathbf{L}' [\hat{\mathbf{H}}_{pp} - \hat{\mathbf{H}}_{ap} \quad \hat{\mathbf{H}}_{pa} - \hat{\mathbf{H}}_{aa}] = [\hat{\mathbf{H}}_{pp} \quad \hat{\mathbf{H}}_{pa}] \quad (19)$$

In this expression the left part results in

$$\mathbf{H}_{d,pp} = \hat{\mathbf{H}}_{pp} + \mathbf{H}_{d,pp} \mathbf{L}' (\hat{\mathbf{H}}_{pp} - \hat{\mathbf{H}}_{ap}) \quad (20)$$

The right part of Eq. (18) leads to

$$\mathbf{H}_{d,pp} \mathbf{L}' = -\hat{\mathbf{H}}_{pa} (\hat{\mathbf{H}}_{pa} - \hat{\mathbf{H}}_{aa})^{-1} \quad (21)$$

Merging the expression given by Eq. (20) into Eq. (19) yields:

$$\mathbf{H}_{d,pp} = \hat{\mathbf{H}}_{pp} - \hat{\mathbf{H}}_{pa} (\hat{\mathbf{H}}_{pa} - \hat{\mathbf{H}}_{aa})^{-1} (\hat{\mathbf{H}}_{pp} - \hat{\mathbf{H}}_{ap}) \quad (22)$$

According to Eq. (43) in Ref. [29], the following relationship exists:

$$[\mathbf{H}_{d,mp} \quad 0] \left(\mathbf{I} - \begin{bmatrix} \mathbf{L}' & -\mathbf{L}' \\ -\mathbf{L}' & \mathbf{L}' \end{bmatrix} \right)^{-1} \begin{bmatrix} \mathbf{H}_{c,pp} & \mathbf{H}_{c,pa} \\ \mathbf{H}_{c,ap} & \mathbf{H}_{c,aa} \end{bmatrix} = [\mathbf{H}_{c,mp} \quad \mathbf{H}_{c,ma}] \quad (23)$$

The second decoupled frequency response can be obtained:

$$\mathbf{H}_{d,mp} = \mathbf{H}_{c,mp} - \mathbf{H}_{c,ma} (\mathbf{H}_{c,aa} - \mathbf{H}_{c,pa})^{-1} (\mathbf{H}_{c,ap} - \mathbf{H}_{c,pp}) \quad (24)$$

Taking into account the above, if the point 'm' on the passive side is considered as the target degree of freedom, the decoupled frequency response can be obtained from Eq. (24), with the corresponding scenario illustrated in Fig. 2(a). Conversely, if the interface

degree of freedom ‘p’ on the passive side is selected as the target, the decoupled frequency response is derived from Eq. (22), as depicted in Fig. 2(b). It is evident that Eq. (22) requires the measurement of fewer quantities compared to Eq. (24), making the transfer function derived from Eq. (22) more advantageous for experimental purposes. This benefit extends to reducing the number of sensors needed and simplifying the measurement process. To substantiate this conclusion, we provide an experimental validation with practical examples in the following sections.

In light of the preceding discussion, the selection of the point of interest on the passive side significantly influences the decoupling process in frequency response analysis. When point ‘m’ on the passive side is targeted, the decoupled frequency response is obtained from Eq. (24), as illustrated in Fig. 2(a). Alternatively, targeting the interface degree of freedom ‘p’ on the passive side yields the decoupled frequency response from Eq. (22), depicted in Fig. 2(b). Notably, Eq. (22) necessitates measuring fewer quantities than Eq. (24), rendering the transfer function from Eq. (22) more practical for experimental applications. This advantage is further amplified by the reduced need for sensors and the simplification of the measurement process. The subsequent sections of this paper will provide experimental validation of these assertions, supported by practical examples.

The generalized virtual decoupling method introduced herein enables the determination of the frequency response of decoupled subsystems without system disassembly. This method demonstrates low sensitivity to the points of force application and sensor placement. In instances of experimentally inaccessible areas, proximal points can be selected, albeit with the understanding that this might introduce minor deviations from the actual conditions, which are generally within acceptable limits [28].

However, the accuracy of Frequency Response Functions (FRFs) [36] derived using virtual decoupling methods during experiments can be a challenge, as they may deviate from the true conditions. To approximate the true FRFs as closely as possible, it is often necessary to conduct multiple measurements at closely located points. A critical task is to establish a quantitative measure for the similarity between the frequency responses, employing representative normalized values to evaluate their accuracy across specific frequency ranges. This approach enables a deterministic assessment of the accuracy of the decoupled frequency responses. In this study, we utilize the Frequency Response Assurance Criterion (FRAC) as a metric to quantify the similarity between the frequency responses obtained from both physical and virtual decoupling methods.

$$FRAC = \frac{\left| \sum_{j=1}^{N_f} (\mathbf{H}_m(\omega_j)^H \cdot \mathbf{H}_M(\omega_j)) \right|^2}{\left[\sum_{j=1}^{N_f} (\mathbf{H}_m(\omega_j)^H \cdot \mathbf{H}_m(\omega_j)) \right] \left[\sum_{j=1}^{N_f} (\mathbf{H}_M(\omega_j)^H \cdot \mathbf{H}_M(\omega_j)) \right]} \quad (25)$$

where the superscript \mathbf{H} represents the Hamiltonian transformation (i.e., the transpose of complex conjugations), the subscripts m and M indicate two points that are located very close together and N_f and ω represent discrete numbers and circular frequencies in the frequency domain, respectively.

2.3. Identification of bearing force

According to the gearbox transfer path modeling shown in Section 2.2, the bearing force can be identified using the vibration response signal and the coupled transfer function matrix. In most cases, transfer function matrices are ill-conditioned matrices. In order to solve the ill-conditioned inverse problem in dynamics, the iterative weighted decomposition and the ill-conditioned coefficient matrix of the weighted control system are used to avoid the matrix inversion in the process of solving and reconstruction. The theory of the Maximally Weighted Iteration (MWI) [35] to identify the bearing force is given below.

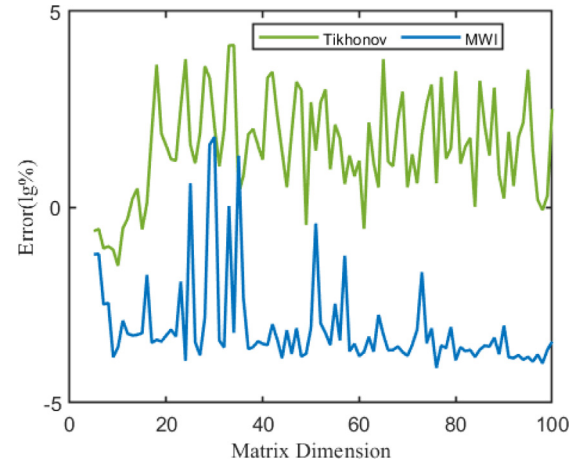


Fig. 4. The errors of solving inverse problems by MWI and Tikhonov for different matrix dimensions.

Taking the result of Eq. (24) as an example, the result of Eq. (22) is similar. The vibration response at the measuring point is modified as:

$$\mathbf{H}_{d,mp}^T \mathbf{x}_m = \mathbf{H}_{d,mp}^T \mathbf{H}_{d,mp} \mathbf{F} \quad (26)$$

Due to inherent rounding errors in computational systems and the presence of observational noise in practical inverse problems, disturbances become unavoidable. Consequently, it becomes imperative to devise numerical techniques aimed at mitigating the ill-conditioning inherent in inverse problems. For the cases that $m < p$, the $\mathbf{H}_{d,mp}^T \mathbf{H}_{d,mp}$ does not exist, and the least square cannot be used to solve the ill-conditioned problem. Considering the singular value decomposition of $\mathbf{H}_{d,mp}$, i.e., $\mathbf{H}_{d,mp} = \mathbf{USV}^*$, in which S is a diagonal matrix of singular values, U and V are unitary matrices, and the superscript ‘*’ denotes conjugate transpose. Among the most renowned approaches is Tikhonov regularization. This method replaces the linear system by the regularized system:

$$(\mathbf{H}_{d,mp}^T \mathbf{H}_{d,mp} + \lambda \mathbf{I}) \mathbf{F} = \mathbf{H}_{d,mp}^T \mathbf{x} \quad (27)$$

where \mathbf{I} indicates a unit matrix. By performing singular value decomposition on $\mathbf{H}_{d,mp}$ and substituting it into Eq. (27), the regularization solution \mathbf{F} can be expressed as:

$$\mathbf{F} = \mathbf{V}(\mathbf{S}^* \mathbf{S} + \lambda \mathbf{I})^{-1} \mathbf{S}^* \mathbf{U}^* \mathbf{x} \quad (28)$$

where λ denotes the regularization parameter. To our knowledge, Tikhonov regularization uses λ to regulate the small singular values. However, for seriously ill-conditioned matrix, too small singular values will lead to rounding in the computing process, and the generalized inverse cannot give a satisfactory solution.

Then the bearing force \mathbf{F} is identified by weighted iterative algorithm. First, a weighted decomposition of \mathbf{F} is performed, that is, $\mathbf{F} = \mathbf{W}\mathbf{f}$. Plug in the above formula:

$$\mathbf{H}_{d,mp}^T \mathbf{x}_m = \mathbf{H}_{d,mp}^T \mathbf{H}_{d,mp} \mathbf{W}\mathbf{f} \quad (29)$$

where \mathbf{W} represents a specially selected non-singular weighted matrix, which can be used to control the pathological degree of $\mathbf{H}_{d,mp}^T \mathbf{H}_{d,mp}$, by acting on the column space of the coefficient matrix $\mathbf{H}_{d,mp}^T \mathbf{H}_{d,mp}$, directly regulates its numerical singularity. The significance of weighting is to change the coefficient matrix in the process of solving and avoid matrix inversion in the process of reconstruction.

For simplicity, let the weighting matrix be $\mathbf{W} = \text{diag}(W_1, W_2, \dots, W_m)$, where m is a positive integer greater than or equal to 2. In order to find an acceptable weighting matrix, some constraints should be satisfied.

Next, we analyze the least upper bound of the inverse error identical with Yu [34] to give guidelines about choosing \mathbf{W} . The selection of the weighted matrix \mathbf{W} is based on the principle of error propagation and amplification, aiming to minimize the upper bound of the error. let $\mathbf{A} = \mathbf{H}_{d,mp}^T \mathbf{H}_{d,mp}$, $\mathbf{Y} = \mathbf{H}_{d,mp}^T \mathbf{x}_m$, $\delta\mathbf{Y}$, $\delta\mathbf{A}$, $\delta\mathbf{F}$ represent the output error, the error of the coefficient matrix \mathbf{A} , and the input error respectively. Assuming that the error is limited, $\bar{\mathbf{Y}}$, $\bar{\mathbf{A}}$, $\bar{\mathbf{F}}$ is used to represent the output, coefficient matrix and input obtained by actual measurement. Then the minimum upper bound of the relative error of the unweighted matrix can be expressed as:

$$\frac{\|\delta\mathbf{F}\|}{\|\mathbf{F}\|} \leq k(\bar{\mathbf{A}}) \frac{\|\mathbf{A}\| \|\delta\mathbf{Y}\|}{\|\mathbf{A}\| \|\mathbf{Y}\|} + k(\bar{\mathbf{A}}) \frac{\|\delta\mathbf{A}\|}{\|\mathbf{A}\|} \quad (30)$$

where $k(\bar{\mathbf{A}}) = \|\bar{\mathbf{A}}\| \|\bar{\mathbf{A}}^{-1}\|$ is the condition number of the matrix $\bar{\mathbf{A}}$. The condition number is usually used to assess the ill-condition degree of the matrix.

Proof. From the definition $\bar{\mathbf{Y}} = \bar{\mathbf{A}}\bar{\mathbf{F}}$, namely:

$$\mathbf{A} + \delta\mathbf{Y} = \mathbf{A}(\mathbf{F} + \delta\mathbf{F}) \quad (31)$$

$$\mathbf{Y} + \delta\mathbf{Y} = (\mathbf{A} + \delta\mathbf{A})\mathbf{F} + \bar{\mathbf{A}}\delta\mathbf{F} \quad (32)$$

From the definition $\mathbf{Y} = \mathbf{A}\mathbf{F}$, namely:

$$\bar{\mathbf{A}}\delta\mathbf{F} = \delta\mathbf{Y} - \delta\mathbf{A}\mathbf{F} \quad (33)$$

Multiply both sides by the generalized inverse matrix of $\bar{\mathbf{A}}$:

$$\delta\mathbf{F} = \bar{\mathbf{A}}^{-1} \delta\mathbf{Y} - \bar{\mathbf{A}}^{-1} \delta\mathbf{A}\mathbf{F} \quad (34)$$

Considering compatibility conditions and triangle inequality of Eq. (32):

$$\|\delta\mathbf{F}\| \leq \|\bar{\mathbf{A}}^{-1}\| \|\delta\mathbf{Y}\| + \|\bar{\mathbf{A}}^{-1}\| \|\delta\mathbf{A}\| \|\mathbf{F}\| \quad (35)$$

The least upper bound of the relative error can be reached when $\|\mathbf{Y}\| = \|\mathbf{A}\| \|\mathbf{F}\|$:

$$\frac{\|\delta\mathbf{F}\|}{\|\mathbf{F}\|} \leq \|\bar{\mathbf{A}}^{-1}\| \|\bar{\mathbf{A}}\| \frac{\|\delta\mathbf{Y}\|}{\|\mathbf{Y}\|} + \|\bar{\mathbf{A}}^{-1}\| \|\delta\mathbf{A}\| \quad (36)$$

From the definition of condition number $k(\bar{\mathbf{A}}) = \|\bar{\mathbf{A}}\| \|\bar{\mathbf{A}}^{-1}\|$, Eq. (34) can be written as:

$$\frac{\|\delta\mathbf{F}\|}{\|\mathbf{F}\|} \leq k(\bar{\mathbf{A}}) \frac{\|\mathbf{A}\| \|\delta\mathbf{Y}\|}{\|\mathbf{A}\| \|\mathbf{Y}\|} + k(\bar{\mathbf{A}}) \frac{\|\delta\mathbf{A}\|}{\|\mathbf{A}\|} \quad (37)$$

The proof is finished.

Multiplying the weighted matrix \mathbf{W} and the matrix $\bar{\mathbf{A}}$, we can obtain the upper bound of the identification error using Eq. (28) as below:

$$\frac{\|\delta\mathbf{F}\|}{\|\mathbf{F}\|} \leq k(\bar{\mathbf{A}}\bar{\mathbf{W}}) \frac{\|\mathbf{A}\| \|\delta\mathbf{Y}\|}{\|\mathbf{A}\| \|\mathbf{Y}\|} + k(\bar{\mathbf{A}}\bar{\mathbf{W}}) \frac{\|\delta\mathbf{A}\|}{\|\mathbf{A}\|} \quad (38)$$

To ensure that the upper bound of the recognition error is reduced after weighted iteration, comparing Eq. (37) with Eq. (38), the following constraints are given [35]:

$$k(\bar{\mathbf{A}}\bar{\mathbf{W}}) < k(\bar{\mathbf{A}})k(\bar{\mathbf{A}}\bar{\mathbf{W}}) \frac{\|\mathbf{W}\| \|\mathbf{A}\|}{\|\bar{\mathbf{W}}\| \|\bar{\mathbf{A}}\|} \leq k(\bar{\mathbf{A}}) \frac{\|\mathbf{A}\|}{\|\bar{\mathbf{A}}\|} \quad (39)$$

Based on constraints Eqs. (28)–(30), for 1-norm, the weighted matrix in the form of column standardization is proposed:

$$\mathbf{W} = diag(W_1, W_2, \dots, W_m), W_i = \sqrt{\left(\sum_{j=1}^m |a_{ij}|^2\right)^{-1}}, i = 1, 2, \dots, m \quad (40)$$

where a_{ij} represents the elements of matrix \mathbf{A} . To further address the issue of ill-conditioned, especially in cases where the number of output channels is less than the number of input channels (underdetermined problems), add a term αf to both sides of the equation:

Next, add a term αf to both sides of the equation:

$$\mathbf{H}_{d,mp}^T \mathbf{x}_m + \alpha f = (\mathbf{H}_{d,mp}^T \mathbf{H}_{d,mp} \mathbf{W} + \alpha) f \quad (41)$$

where α is the weighting factor, which can be calculated by Lcurve criterion or generalized cross-validation (GCV) method [36]. This addition helps to avoid rank deficiency in the coefficient matrix, thereby stabilizing the numerical solution process. When $\alpha > 0$, the pathological degree of the symmetric matrix $\mathbf{H}_{d,mp}^T \mathbf{H}_{d,mp} \mathbf{W}$ is further reduced. Assuming convergence to f after k iterations, Eq. (41) is rewritten into a coefficient matrix of the following iteration form:

$$\mathbf{H}_{d,mp}^T \mathbf{x}_m + \alpha f^k = (\mathbf{H}_{d,mp}^T \mathbf{H}_{d,mp} \mathbf{W} + \alpha) f^{(k+1)} \quad (42)$$

Finally, the identified bearing force is further expressed as:

$$\mathbf{F} = \mathbf{W} f^k \quad (43)$$

In summary, the steps of calculating bearing force according to the MWI can also refer to Algorithm 1. The algorithm first initialize the formula and weighted matrix in Line 3 and Line 4, then an iterative process is used to find the optimal force estimation in Line 6–9. To test the accuracy of the proposed MWI approach, the incision errors are calculated for 100 different inputs to represent the accuracy of Tikhonov and MWI, as shown in Fig. 4. The primary advantage of MWI over Tikhonov regularization lies in the consistency of the solution, as demonstrated in Ref. [35]. This characteristic ensures that the time-domain waveforms of bearing dynamic forces can be accurately reconstructed from the identified spectra, free from the systematic bias introduced by the regularization term. Although Tikhonov regularization may yield higher identification accuracy for large matrix dimensions or highly ill-conditioned problems, it lacks the solution consistency offered by MWI.

Algorithm 1 Maximally Weighted Iteration for bearing force identification

- 1: **Input:** Vibration response signals \mathbf{x}_m ; Transfer function matrix $\mathbf{H}_{d,mp}$; The maximumly number of iterations K .
- 2: **Output:** Bearing force $\mathbf{F} = \mathbf{W} f$.
- 3: Initialize the formulae: $\mathbf{H}_{d,mp}^T \mathbf{x}_m = \mathbf{H}_{d,mp}^T \mathbf{H}_{d,mp} \mathbf{W} f$
- 4: Initialize the weighted matrix \mathbf{W} in Eq. (31), considering the constraints in Eq. (28)–(30).
- 5: Choose the weighted factor α by GCV.
- 6: **for** $k=1,2,\dots,K$. **do**
- 7: $\mathbf{H}_{d,mp}^T \mathbf{x}_m + \alpha f^k = (\mathbf{H}_{d,mp}^T \mathbf{H}_{d,mp} \mathbf{W} + \alpha) f^{(k+1)}$
- 8: $f^k \leftarrow f$.
- 9: **Until** $k \geq K$
- 10: **end for**

3. Transfer path contribution and simulation verification

In the section, we investigate the properties of physical decoupling and virtual decoupling and compare the performance of bearing forces identification between the proposed virtual decoupling method and the method shown in [30]. Taking the dynamic model of a two-stage parallel shaft gear transfer system as an example, the specific process of transfer path analysis is illustrated. Simultaneously, the effectiveness of the proposed decoupling method is validated through numerical examples, in which a lumped parameter dynamic model shown in Section 2.1 is used to provide theoretical coupled and decoupled frequency

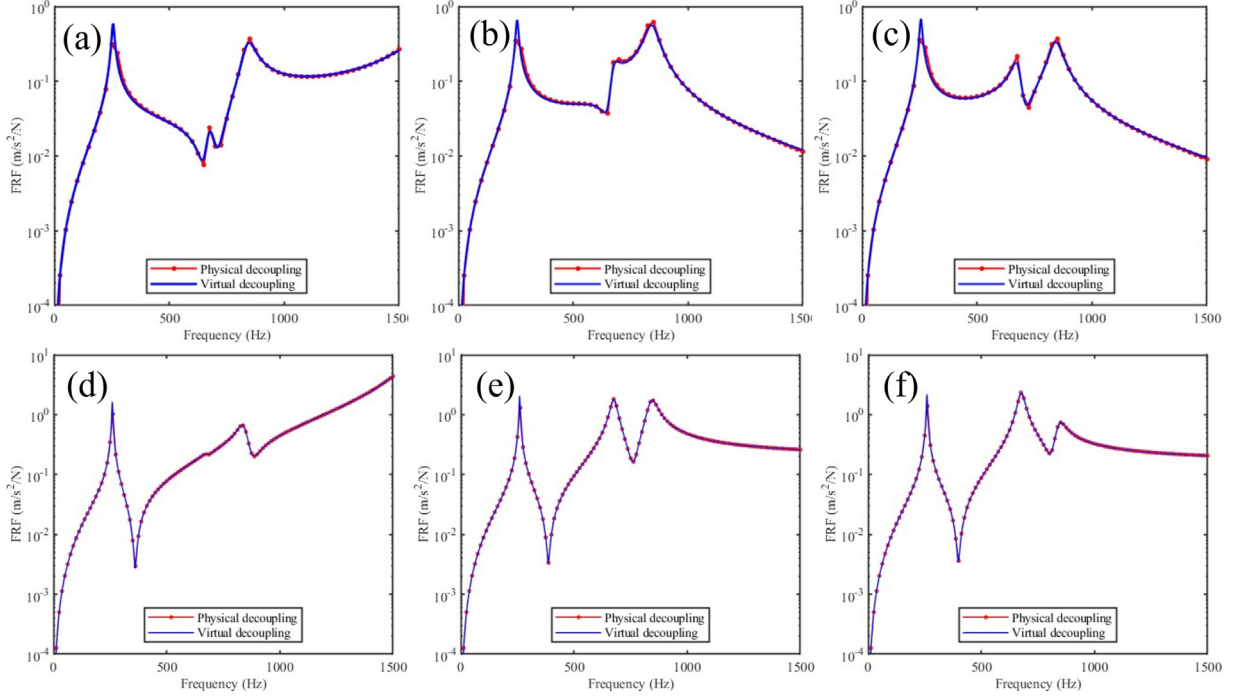


Fig. 5. Comparison of FRF between the physical decoupling and two virtual decoupling methods. (1) $H_{d,mp}$: (a) H_{47} , (b) H_{57} , (c) H_{67} ; (2) $H_{d,pp}$: (d) H_{47} , (e) H_{57} , (f) H_{67} .

Table 1
Main parameters of the numerical example.

Parameters	Value	Parameters	Value
Number of teeth	$Z_1 = 28, Z_2 = 40, Z_3 = 34, Z_4 = 34$	Density (kg/m^3)	7850
Young's modulus (GPa)	210	Radius of the shaft (mm)	24
Poisson's ratio	0.3	Module (mm)	3
Face width (mm)	16	Pressure angle ($^\circ$)	20
Addendum coefficient	1	Bottom clearance coefficient	0.3
Mass (kg)	$M_4 = 1, M_5 = 2, M_3 = 3, M_7 = 23.5$	Damping ratio	0.02
Damp (N s/m)	$c_{36} = 1e4, c_{25} = 1e4, c_{14} = 1e4$	Stiffness (N/m)	$k_{36} = 1e7, k_{25} = 1e7$
Damp (N s/m)	$c_{47} = 1e3, c_{57} = 1e3, c_{67} = 1e3$	Stiffness (N/m)	$k_{14} = 1e7$
Stiffness (N/m)	$k_{57} = 1e8, k_{67} = 1e8$	Stiffness (N/m)	$k_{47} = 1e8$

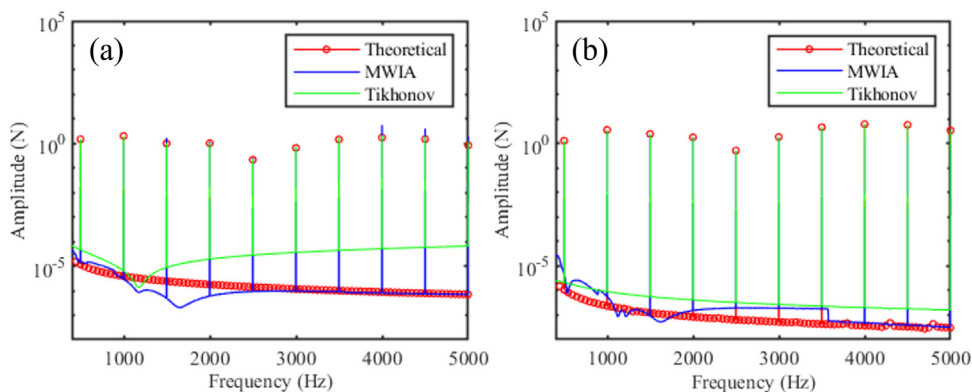


Fig. 6. Compared with Ref. [30], bearing forces identified in a single-stage gearbox system through theoretical identification and two algorithmic identifications: (a) F_1 ; (b) F_2 .

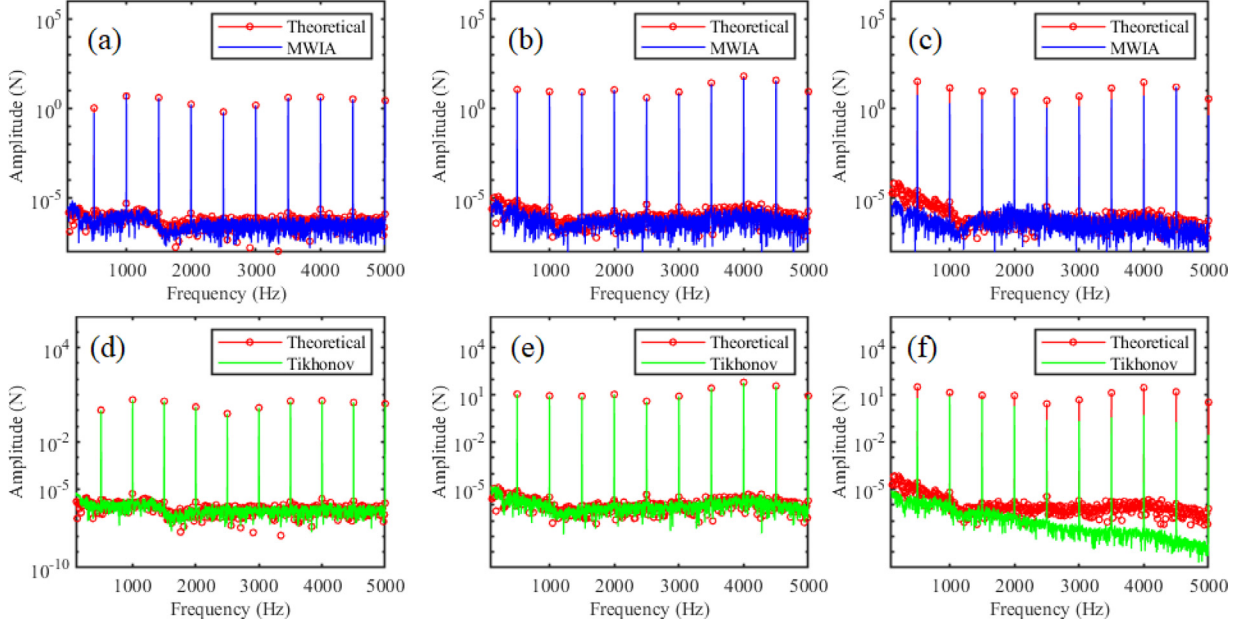


Fig. 7. Bearing forces identified in a two-stage gearbox system through theoretical identification and two algorithmic identifications: (a,d) F_4 ; (b,e) F_5 ; (c,f) F_6 .

response functions (using Eqs. (6) and (7)). The parameters of the numerical examples are shown in Table 1.

The frequency response function of physical decoupling can be obtained from the matrix of the non-source part (using Eq. (6)). Virtual decoupling refers to calculating the decoupled frequency response using the matrix of the entire coupled system. The method proposed in this paper calculates the virtual decoupled frequency response using the matrix of the entire coupled system when the matrix of the passive part is unknown (using Eqs. (22) and (24)). The obtained virtual decoupled frequency response is compared with the frequency response obtained from physical decoupling, as shown in Fig. 5. It is found that the two are basically consistent, thereby validating the generalized virtual decoupling method proposed in this paper.

As shown in Fig. 3(left), there are three transfer paths connecting the active part and the passive part. Measuring the vibration response at masses 4, 5 and 6 can determine the interface force \mathbf{F} . Theoretically, the bearing force subjected to the three masses can be expressed as:

$$\begin{aligned} F_4 &= k_{14}(x_1 - x_4) + c_{14}(\dot{x}_1 - \dot{x}_4) \\ F_5 &= k_{25}(x_2 - x_5) + c_{25}(\dot{x}_2 - \dot{x}_5) \\ F_6 &= k_{36}(x_3 - x_6) + c_{36}(\dot{x}_3 - \dot{x}_6) \end{aligned} \quad (44)$$

here k represents the meshing stiffness matrix between the two masses, c represents the damping matrix between the two masses, and x represents the displacement matrix between the two degrees of freedom.

In the process of solving the inverse problem, the bearing forces identified by the proposed MWI and Tikhonov are compared and analyzed. Similar to literature [30], the bearing force identified in the first-stage gearbox is first given. As shown in Fig. 6, in the comparison between the bearing force obtained theoretically and the identified bearing force, it can be seen that both methods can achieve the ideal accuracy of identifying bearing force, and the error is within a small amplitude range, which makes little contribution to the system. However, in the high frequency part, the MWI is more accurate than the Tikhonov method to identify bearing forces of different paths. In the two-stage gear box, as shown in Fig. 7, the accuracy of the bearing forces F_4 and F_5 identified by the two methods is close to each other. From the identified bearing force F_6 , it is obvious that the proposed MWI is more accurate in the high frequency part. To sum up, the average relative error for MWI is one order of magnitude, and that for Tikhonov is 1–3 orders of magnitude. Then, the noise-robustness of

Table 2

Relative errors of the Tikhonov and MWI for different signal to ratio.

	Random noise	0.0001	0.001	0.01
Tikhonov	1.92%	17.28%	325.53%	
MWI	0.05%	0.11%	7.62%	

MWI to random noise is also tested. For different noise level, the mean value and standard deviation of the noise are equal to the random noise value in Table 2. The relative error results of Table 2 point to the same conclusion: MWI is more robust to noise than the Tikhonov, especially for the matrix with a higher ill-conditioned degree. This also proves the superiority of the MWI in solving ill-conditioned matrix problems.

According to the virtual decoupled transfer function and recognition bearing force obtained above, path contribution can quantitatively reflect the contribution of each transfer path. Therefore, the vibration response at the measuring point ‘m’ or ‘p’ can be expressed as the superposition of the contributions of each transfer path:

$$\mathbf{X}_m = \mathbf{H}_{d,mp}\mathbf{F} = \sum_i^n \mathbf{H}_{d,mpi}\mathbf{F}_i \quad \text{or} \quad \mathbf{X}'_m = \mathbf{H}_{d,pp}\mathbf{F}' = \sum_i^n \mathbf{H}_{d,ppi}\mathbf{F}'_i \quad (45)$$

4. Experimental verification

In this section, we experimentally validated the effectiveness of the proposed method in the practical diagnosis of faults in gearbox systems. The two-stage parallel-axis gearbox test rig, as shown in Fig. 8, and the gearbox parameters listed in Table 1 were utilized for the experiments. Vibration signals were measured using six triaxial accelerometers (DH-1A339E), with these locations marked in yellow. Gears on the shaft could be replaced, corresponding to three types of faults: chipped tooth, localized wear, and tooth fracture. The characteristic frequencies of gear faults were defined as the meshing frequencies modulated by the shaft and the faulty gear pair.

Six triaxial accelerometers were installed on both sides of the gearbox. Since axial forces could be neglected for spur gears, the experiment only involved the x and y directions. The two-stage parallel-axis gear system comprised 12 transfer paths. Utilizing the proposed generalized virtual decoupling method, frequency response experiments were conducted on the gearbox system, yielding the decoupled frequency

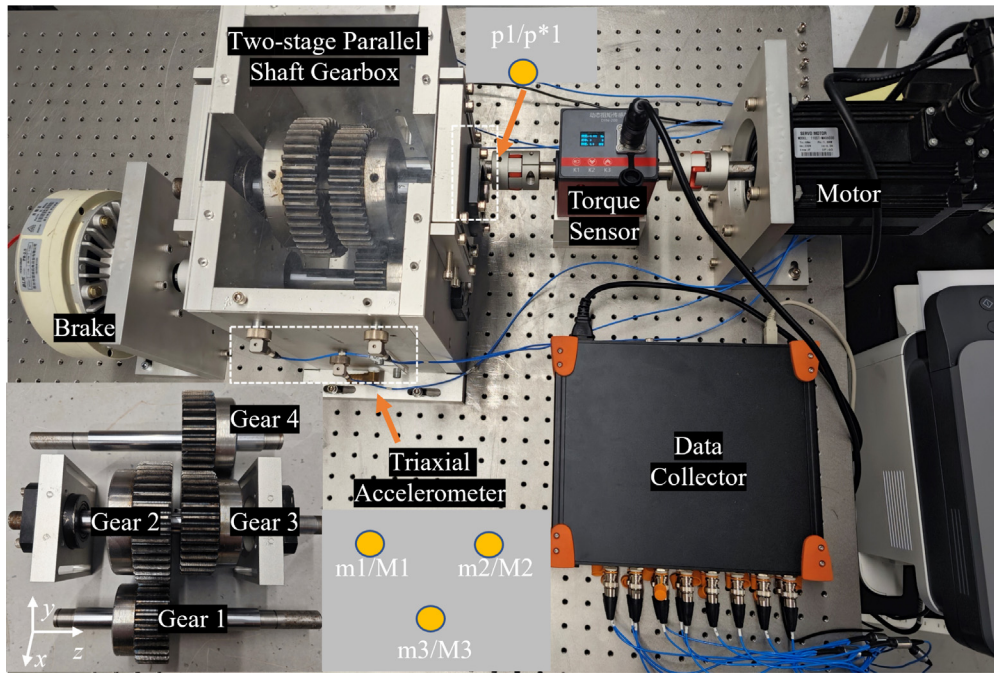


Fig. 8. Two-stage parallel shaft gear test bed in the experiment.

response of the housing. An impact hammer (DH-LC02-3A102) was used to apply impact excitation, with a sampling frequency set at 8000 Hz. The data acquisition device (DH8303) was employed to collect both excitation and response signals. The physical decoupling test results were considered as the benchmark to validate the virtual decoupling method. Additionally, based on frequency response functions and the vibration response of the gearbox housing, the MWI theory was introduced for bearing force identification.

4.1. Virtual decoupling obtains FRF

In the virtual decoupling method proposed in this paper, 12 frequency response parameters can be obtained from a single hammer test. The frequency response matrices required for the two different measurement points are not entirely the same. For $\mathbf{H}_{d,mp}$, the coupled frequency response matrices that need to be measured include $\mathbf{H}_{c,aa}$, $\mathbf{H}_{c,pa}$, $\mathbf{H}_{c,pp}$, $\mathbf{H}_{c,ma}$, and $\mathbf{H}_{c,mp}$. For $\mathbf{H}_{d,pp}$, the coupled frequency response matrices to be measured are only $\mathbf{H}_{c,aa}$, $\mathbf{H}_{c,pa}$ and $\mathbf{H}_{c,pp}$. The coupled frequency response matrices $\mathbf{H}_{c,aa}$, $\mathbf{H}_{c,pa}$ and $\mathbf{H}_{c,pp}$ each require a total of 12 hammer tests along the x and y directions, while the matrices $\mathbf{H}_{c,ma}$ and $\mathbf{H}_{c,mp}$ require one hammer test each. Furthermore, according to the reciprocity principle, the frequency response matrix $\mathbf{H}_{c,pa}$ is equal to $\mathbf{H}_{c,ap}$. The frequency response functions obtained by the virtual decoupling method at measurement point ‘m1’, its neighboring points ‘M1’, and at measurement point ‘m2’ and its neighboring points ‘M2’ are shown in Fig. 9. The frequency response functions obtained at measurement point p1, its neighboring points ‘p1’, and at measurement point ‘p2’ and its neighboring points ‘p2’ are shown in Fig. 10. The corresponding similarity measured by the FRAC value introduced in Section 2.2 is shown in Table 3. It can be observed that the two derived types of decoupled frequency responses are close to their actual values, and the FRAC values between adjacent measurement points are high, indicating that the experimental results are quite accurate. To quantify testing efficiency, Table 4 lists the time costs involved in each test process. It is evident that the virtual decoupling method proposed in this paper reduces the time by more than 70% compared to physical decoupling. Choosing point ‘p’ as the measurement location (with $12 * 3 = 36$ impacts), compared to point ‘m’ (with $12 * 3 + 1 * 2 = 38$

Table 3

The frequency response assurance criterion of the target frequency response and the real value.

	m1/real value	m1/M1	m2/real value	m2/M2
FRAC($\mathbf{H}_{c,mp}$)	0.63345	0.86507	0.88016	0.97531
p1/real value		p1/p*1	p2/real value	p2/p*2
FRAC($\mathbf{H}_{c,pp}$)	0.62683	0.85227	0.80604	0.91434

Table 4

Test and calculation time statistics of object-understanding coupling and two virtual decoupling.

	Dismantle	Hammering test	Assemble	Calculate	Total time
Physical decoupling	100 min	12 min	100 min	10 min	222 min
Virtual decoupling($\mathbf{H}_{c,mp}$)	0 min	38 min	0 min	30 min	68 min
Virtual decoupling($\mathbf{H}_{c,pp}$)	0 min	36 min	0 min	20 min	56 min

impacts), resulted in a reduction of two impacts. This led to a 33% decrease in computational load, consequently shortening the overall required time.

4.2. Transfer path contribution and fault tracing

To enhance the validity of the methodologies proposed in this research for fault tracing and fault feature enhancement, a series of experiments were conducted on a wind turbine gearbox fault simulation test rig. These experiments involved the collection of vibration acceleration signals from measurement points ‘m’ and ‘p’ on the gearbox under stable operating conditions. Subsequently, bearing forces were deduced by analyzing these signals using the decoupled frequency responses derived from Eqs. (22) and (24). This research introduces three distinct types of artificially induced faults: chipped tooth, localized wear, and tooth fracture, as illustrated in Fig. 11. Specifically, a chipped tooth

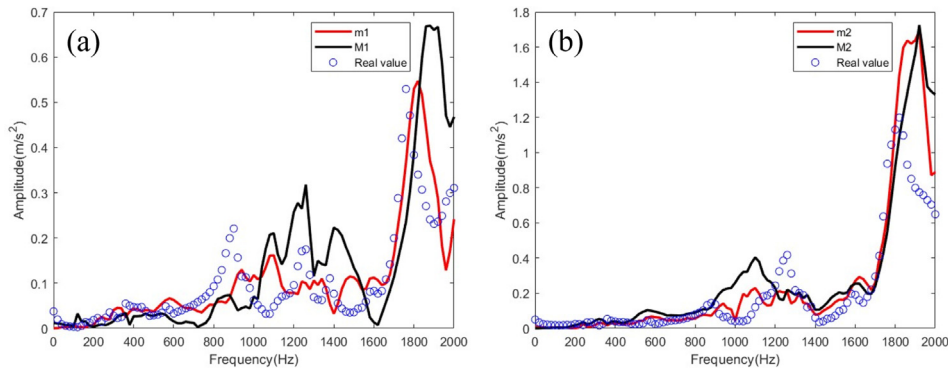


Fig. 9. Comparison of FRF obtained from real value and decoupled value: (a) $H_{m1,p9}$, $H_{M1,p9}$ and relevant real value; (b) $H_{m2,p9}$, $H_{M2,p9}$ and relevant real value.

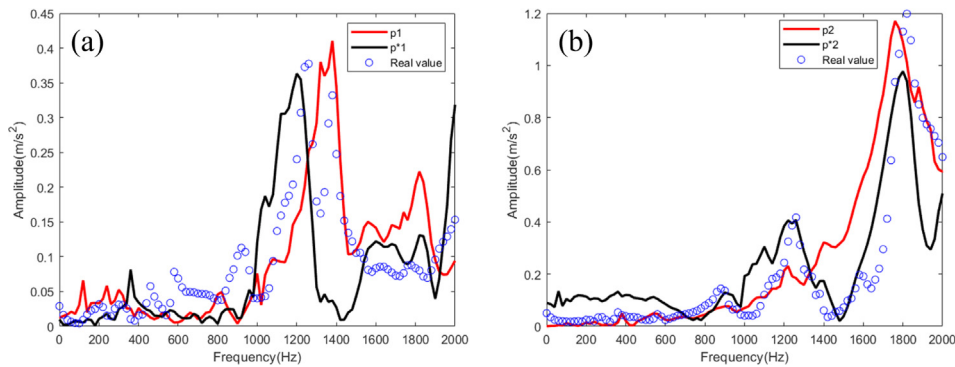


Fig. 10. Comparison of FRF obtained from real value and decoupled value: (a) $H_{p1,p}$, $H_{p^{*1},p}$ and relevant real value; (b) $H_{p2,p}$, $H_{p^{*2},p}$ and relevant real value.

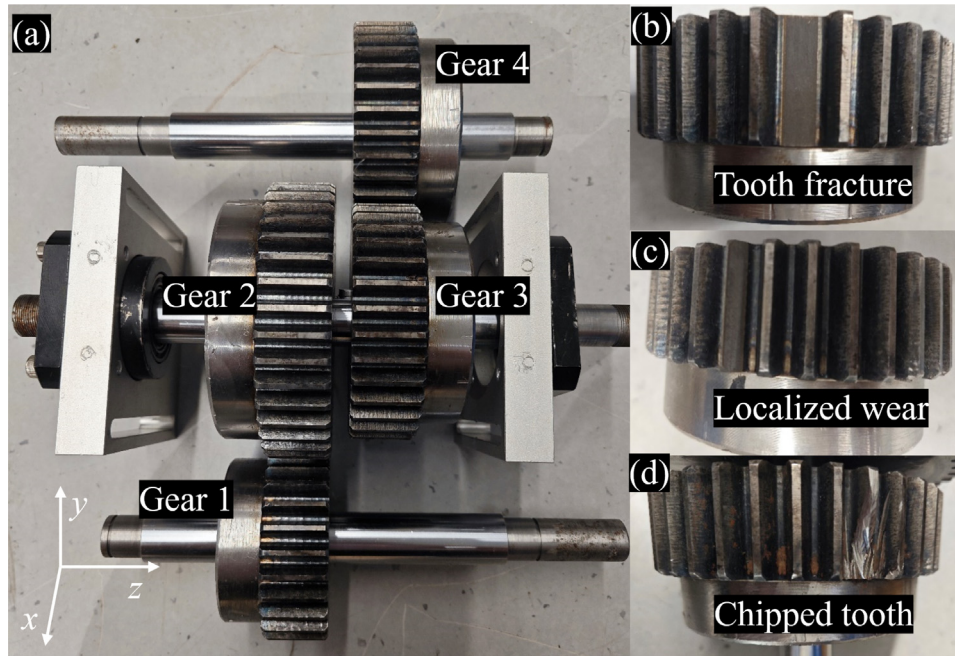


Fig. 11. Gearbox internal structure and different faults.

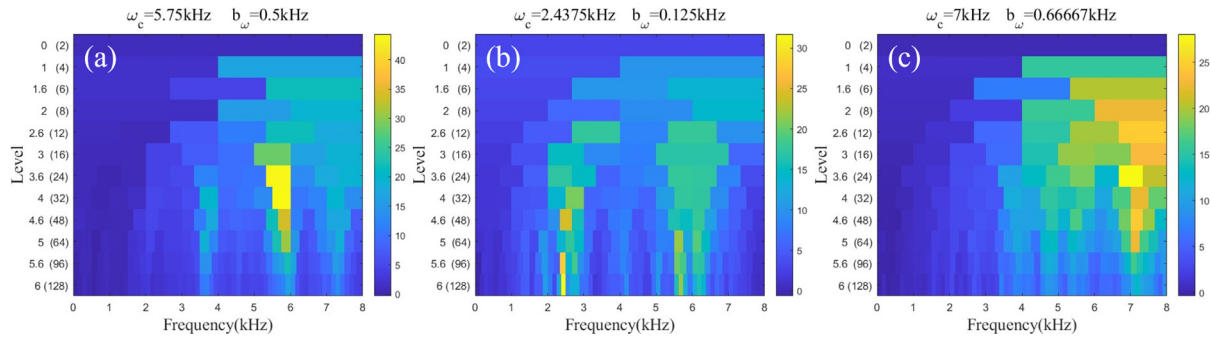


Fig. 12. For FRF $H_{c,mp}$, spectral kurtographs of different fault types at measuring point m: (a) Tooth fracture (b) Localized wear (c) Chipped tooth.

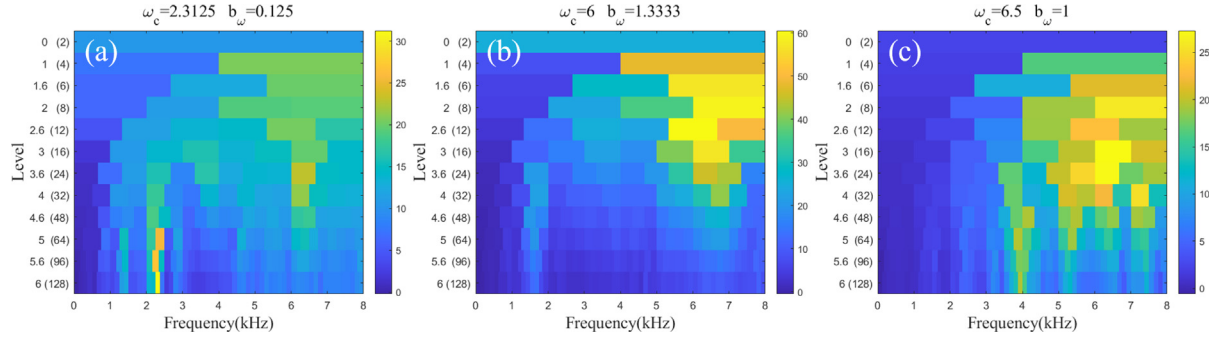


Fig. 13. For FRF $H_{c,pp}$, spectral kurtographs of different fault types at measuring point p: (a) Tooth fracture (b) Localized wear (c) Chipped tooth.

fault entails the removal of 70% of the tooth edge, the localized wear fault involves a wear depth of 0.3 mm, and the tooth fracture fault is characterized by the complete removal of a tooth's height.

Different types of gear faults in gearbox systems are known to produce unique amplitude modulation effects in the frequency spectrum. To enhance the identification of these fault characteristics, this study employs the spectral kurtosis technique. This technique helps in pinpointing transient characteristics of the fault signals gathered at measurement points 'm' and 'p', identifying a bandwidth centered at frequency ω_c with a resonance band b_{ω} , as depicted in Figs. 12 and 13. Summation of path contributions for various fault types allows for the isolation of the path contribution specific to a particular fault type, as illustrated in Figs. 14 and 15.

To be more specific, we first provide an overview of three different types of faults – chipped tooth, localized wear, and tooth fracture – in Fig. 11. Additionally, Figs. 14 and 15 highlight the positions closest to the faulty gear with different colors. For example, in Fig. 11, (a) shows 12 transfer paths. In (b), the 6th transfer path has the highest contribution, indicating that the nearest gear has a fault (corresponding to Gear 2 in Fig. 14). However, the maximum contribution is observed in the 7th or 8th transfer paths, it suggests a fault in Gear 3. In (c), the 9th transfer path has the highest contribution, corresponding to Gear 4 in Fig. 11. Similarly, in (d), the 10th transfer path has the highest contribution, also corresponding to Gear 4 in Fig. 11. The accurate decoupled transfer functions derived from both measurement points 'p' and 'm' confirm the utility of the virtual decoupling method based on transfer path analysis introduced in this paper. This approach offers a distinct advantage in fault tracing by adaptively determining the fault location based on the path contribution.

4.3. Fault feature enhancement

Most existing signal decomposition methods are data-driven and lack emphasis on the physical interpretability of the decomposition

process. However, the generalized virtual decoupling method rooted in transfer path analysis, as proposed in this study, provides a coherent explanation of the signal decomposition process. This method interprets vibration signals collected at measurement points 'm1' and 'p1' as the aggregate of 12 distinct absolute path contributions. By applying bandpass filters designed using the resonance bands and center frequencies previously determined, the filtered output signals are then subjected to demodulation via the Hilbert transform to produce the analytic signal. The procedure of fault feature enhancement is illustrated by Algorithm 2. The virtual decoupled FRF identified bearing force, the algorithm will lead to the enhanced faulty signal. The subsequent step involves extracting the square envelope spectrum of this analytic signal, as illustrated in Figs. 16 and 17.

Algorithm 2 Fault feature enhancement

- Input:** Virtual decoupling for FRF of each transfer path; Identification of the bearing force signal.
- Output:** The square envelope spectrum of the reconstructed signal.
- Calculate the contribution of each transfer path with identified bearing force based on Eq.(36).
- The reconstruction signal is obtained by multiplying the dominant path FRF and its associated bearing force signal.
- Design the bandpass filters with spectral kurtosis method.
- Demodulation analysis of reconstructed signals with Hilbert transform.
- Quantify the fault feature enhancement effect.

In the context of tooth fracture faults, the characteristic fault frequency is identified as $f_1 = 10$ Hz. For faults like localized wear and chipped tooth, the characteristic fault frequency is $f_2 = 7$ Hz. The envelope spectrum analysis, as presented in this study, not only clearly reveals the fault characteristic frequency f_1 but also significantly amplifies its amplitude compared to the original signal (see Fig. 16(a), (b)). This amplification is also evident for the other fault types (localized wear and chipped tooth), as shown in Fig. 16(c)–(f).

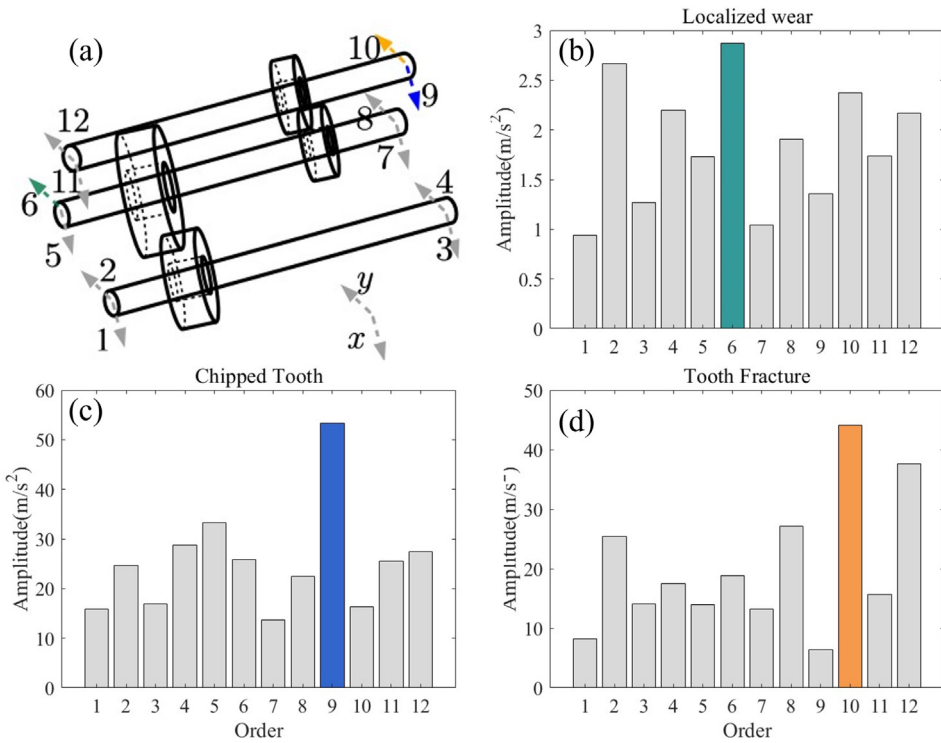


Fig. 14. For FRF $H_{c,mp}$, signal measuring points at different locations (a); Different fault type path contribution: (b) Localized wear; (c) Chipped tooth; (d) Tooth fracture.

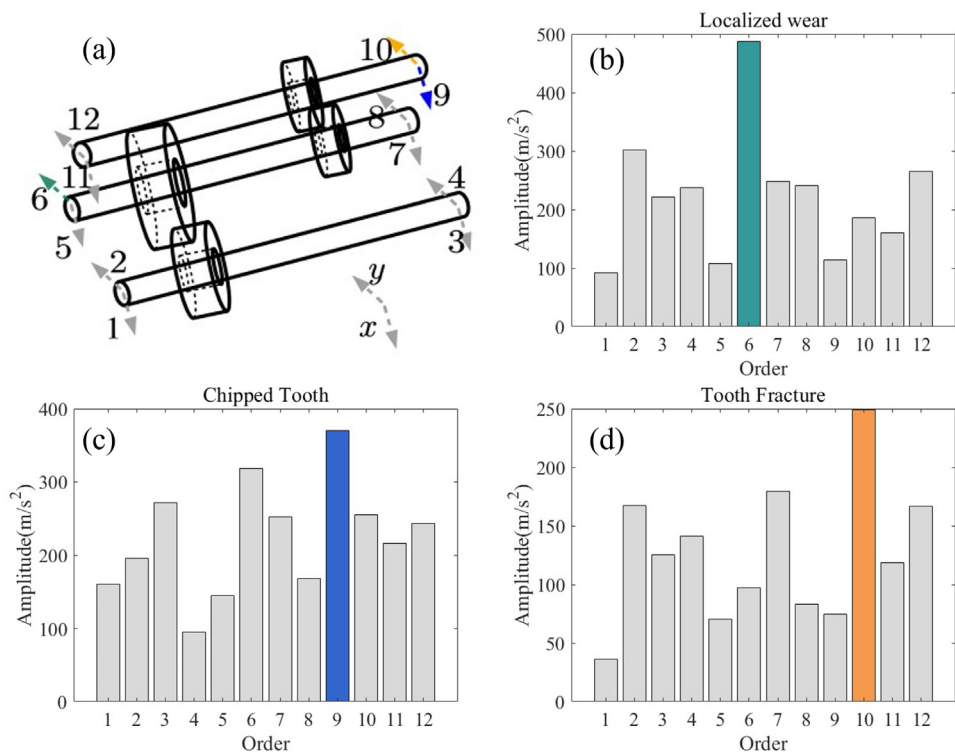


Fig. 15. For FRF $H_{c,pp}$, signal measuring points at different locations (a); Different fault type path contribution: (b) Localized wear; (c) Chipped tooth; (d) Tooth fracture.

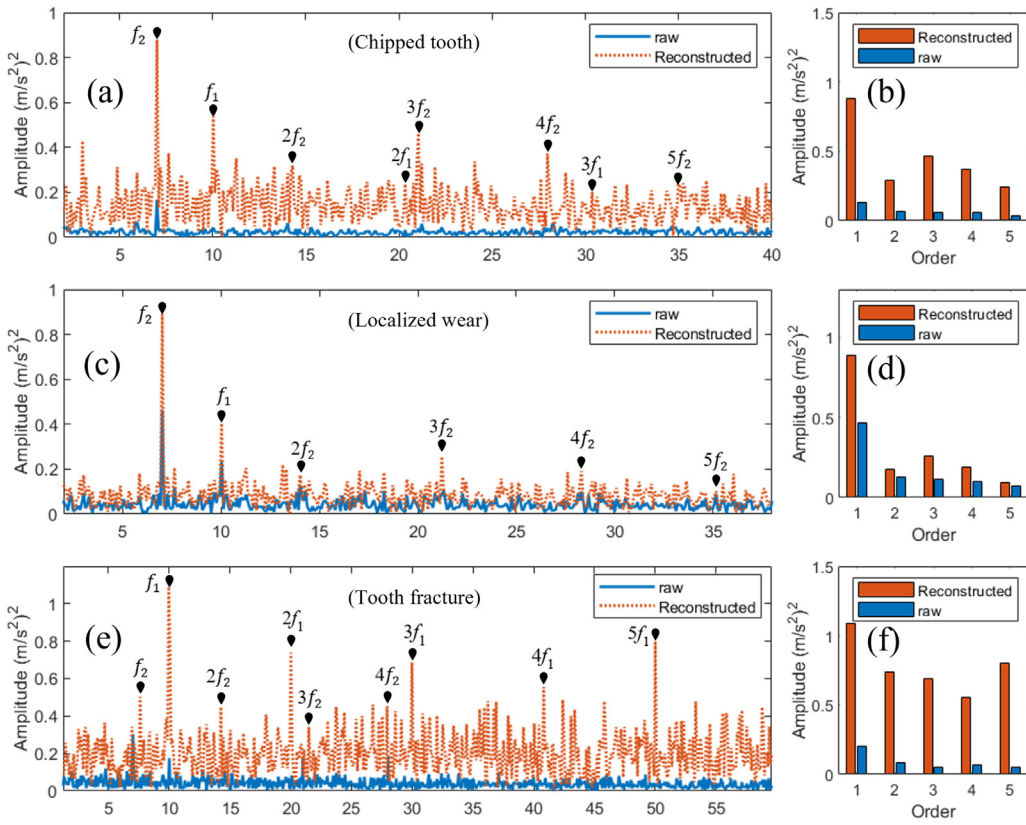


Fig. 16. For FRF $H_{c,\text{mp}}$ at 600 r/min, square envelope spectra of different faults and characteristic order spectra of their frequencies : (a),(b) Chipped tooth; (c),(d) Localized wear; (e),(f) Tooth fracture.

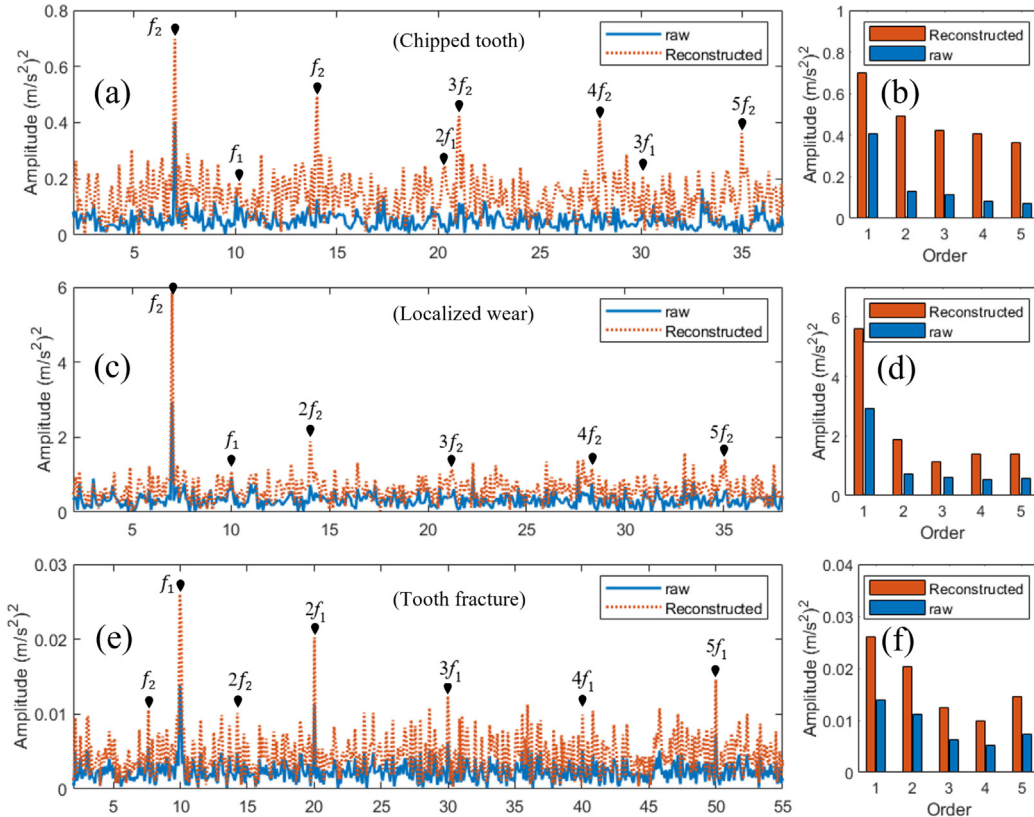


Fig. 17. For FRF $H_{c,\text{pp}}$ at 600 r/min, square envelope spectra of different faults and characteristic order spectra of their frequencies : (a),(b) Chipped tooth; (c),(d) Localized wear; (e),(f) Tooth fracture.

Table 5

Two kinds of decoupled frequency response functions correspond to different kinds of fault characteristics enhanced comparison.

	Localized wear	Tooth fracture	Chipped tooth
$H_{c,mp}$	213%	836%	632%
$H_{c,pp}$	200%	211%	296%

The efficacy of the proposed method in enhancing and extracting fault features is evident, suggesting its potential for significant impact in mechanical fault diagnosis. To quantify the fault feature enhancement, the sum of the amplitudes of the first five characteristic frequencies in the envelope spectrum is used as a fault indicator. This quantification, comparing the fault indices of the original and decomposed signals, underscores the characteristic enhancement achieved through the proposed decomposition method. **Table 5** details the magnification values for each fault type when using measurement points ‘m1’ and ‘p1’. The enhancement of fault features exceeds 200% for all types, demonstrating the method’s capability to extract features from weak fault signals. This improved transfer path analysis method, thus, marks a significant advancement in the field.

The detailed experimental setup and results demonstrating the universality and robustness of the proposed method, tested on various gearbox systems under different operating conditions, can be found in [Appendix A](#). The enhancement of fault characteristics for three distinct fault types is presented, illustrating the method’s strong generalization and robustness.

5. Conclusion

This study advances the field of gearbox fault diagnosis by introducing a new structural dynamics decoupling method based on Transfer Path Analysis (TPA). Our approach not only diagnoses and tracks faults in multi-stage gearbox systems with high efficiency but also provides a robust framework for the identification of critical transfer paths that are pivotal for fault detection. It successfully derives frequency response functions that accurately identify a decoupled system, using these functions alongside vibration response signals to solve the inverse problem of bearing force identification through Maximally Weighted Iteration (MWI) [35]. The MWI method exhibits considerable advantages over the Tikhonov method, particularly in accuracy, noise robustness, the stability and consistency of the solution. These attributes render MWI a highly valuable tool for bearing force identification in engineering applications. The research identifies dominant transfer paths for fault frequencies, enabling effective tracing of gear faults such as wear, tooth breakage, and corner collapse. A signal decomposition method proposed in this study enhances fault characteristics, with tests showing that the fault indicator of various fault types are amplified by more than 200%, confirming the method’s precision in reflecting gearbox faults. Significantly, this method eliminates the need for physical disassembly in multi-stage parallel gear systems, reducing signal measurement points. Finally, experiments were conducted on various types of gearbox systems under different operating conditions. The results indicated a significant enhancement in the features of three distinct fault types, further validating the method’s generalization and robustness.

Future Outlook:

1. The bearing interface is a crucial contact point for the transfer of vibrational energy in gear transfer systems, and there is currently a lack of in-depth study on the signal attenuation and energy transfer processes at the bearing interface. Subsequent research will involve establishing an energy attenuation model for the bearing interface and studying the vibration transfer mechanism at the bearing interface.
2. The method proposed in this paper is primarily aimed at parallel-axis gear transfer systems and is not applicable to planetary

Table 6

The fault characteristic frequencies corresponding to different gearbox rotational speeds.

Rotation frequency(r/min)	600	500	400	300
f_1 (Hz)	10	8.33	6.67	5
f_2 (Hz)	7	5.83	4.669	3.5

gear systems. In planetary gear systems, due to the pass-through effect of the planetary gears, the transfer path has time-variant characteristics. One of the future research directions is to carry out time-variant transfer path analysis for planetary gear transfer systems.

CRediT authorship contribution statement

Penghong Lu: Writing – original draft, Software, Conceptualization, Formal analysis, Data curation. **Cai Li:** Software, Formal analysis, Data curation. **Gang Chen:** Supervision. **Gang Chen:** Writing – review & editing, Validation, Supervision.

Acknowledgments

This work is partially supported by the National Key Research and Development Program of China (Grant No. 2021YFB3301400), the National Science Foundation of China (Grant No.52305105), the Basic and Applied Basic Research Foundation of Guangdong Province (Grant No.2022A1515240027 and No.2023A1515010812), and Guangzhou Research Foundation (Grant No. 2023A04J1582).

Declaration of competing interest

The authors declare the following financial interests/personal relationships which may be considered as potential competing interests: Gang Chen reports financial support was provided by National Science Foundation of China and Basic and Applied Basic Research Foundation of Guangdong Province. If there are other authors, they declare that they have no known competing financial interests or personal relationships that could have appeared to influence the work reported in this paper.

Appendix A. Suggested experimental procedures for evaluating gearbox systems

The primary objective of this appendix is to provide guidance for conducting comprehensive experiments on different types of gearbox systems under various operating conditions. we have conducted comparative experiments at rotational speeds of 300, 400, 500, and 600 r/min, as shown in the [Figs. 18–20](#) and the [Table 6](#). The fault characteristics of the three different fault types have been significantly enhanced, indicating that the method used in this paper has good generality and robustness.

Appendix B. Selection of weight factors in the MWI algorithm

We have selected the weighted iterative factor, α , to be greater than 0. This choice is based on our analysis, which indicates that a positive α effectively improves the conditioning of the matrix and enhances the performance of the MWI algorithm. For giving positive definite symmetric matrix A , when α is greater than 0, the condition number of matrix $A + \alpha E$ is less than that of matrix A .

Proof. Suppose λ_i is a i th eigenvalue of matrix $A + \alpha E$, and λ'_i is a i th eigenvalue of matrix A , then:

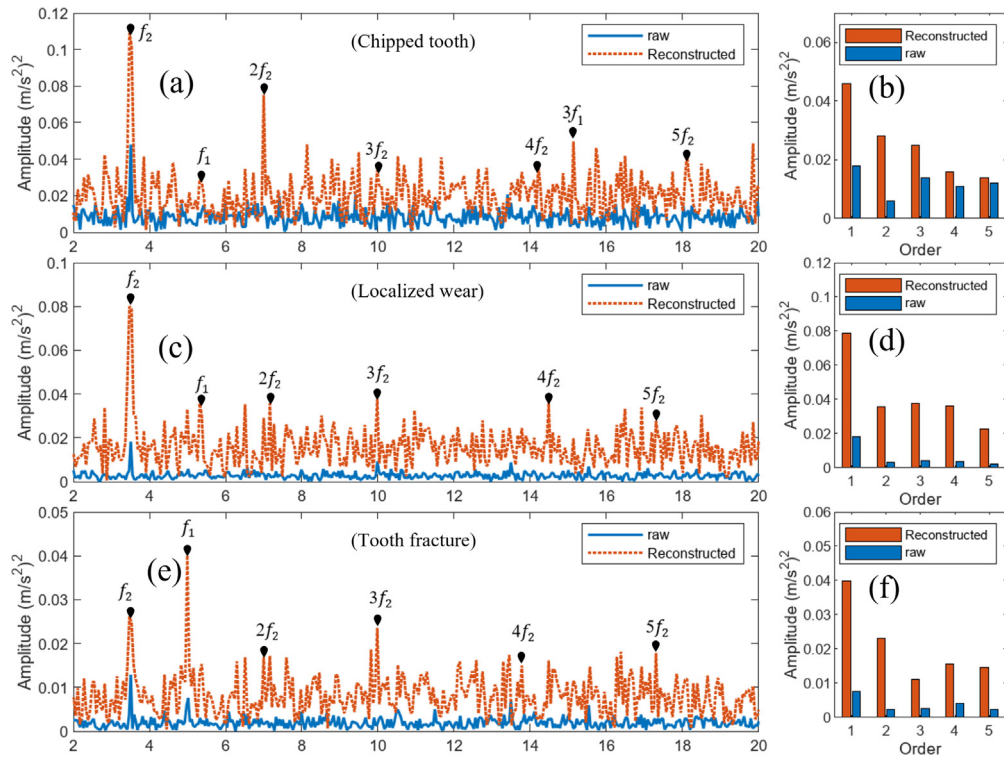


Fig. 18. For FRF $H_{c,pp}$ at 300 r/min, square envelope spectra of different faults and characteristic order spectra of their frequencies : (a),(b) Chipped tooth; (c),(d) Localized wear; (e),(f) Tooth fracture.

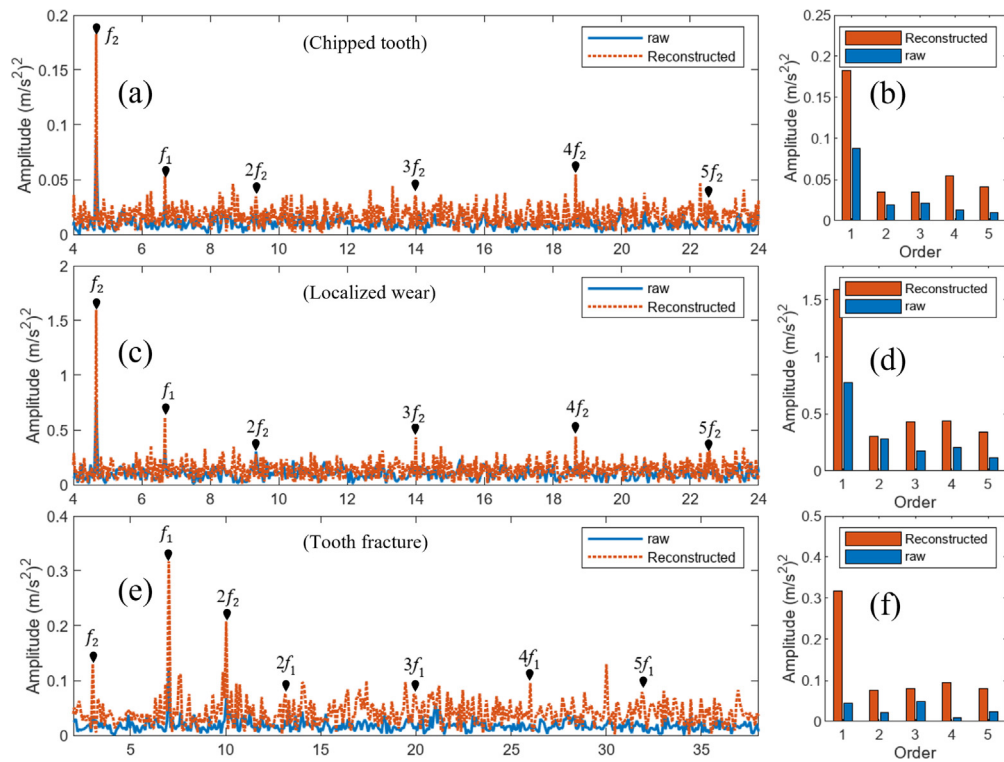


Fig. 19. For FRF $H_{c,pp}$ at 400 r/min, square envelope spectra of different faults and characteristic order spectra of their frequencies : (a),(b) Chipped tooth; (c),(d) Localized wear; (e),(f) Tooth fracture.

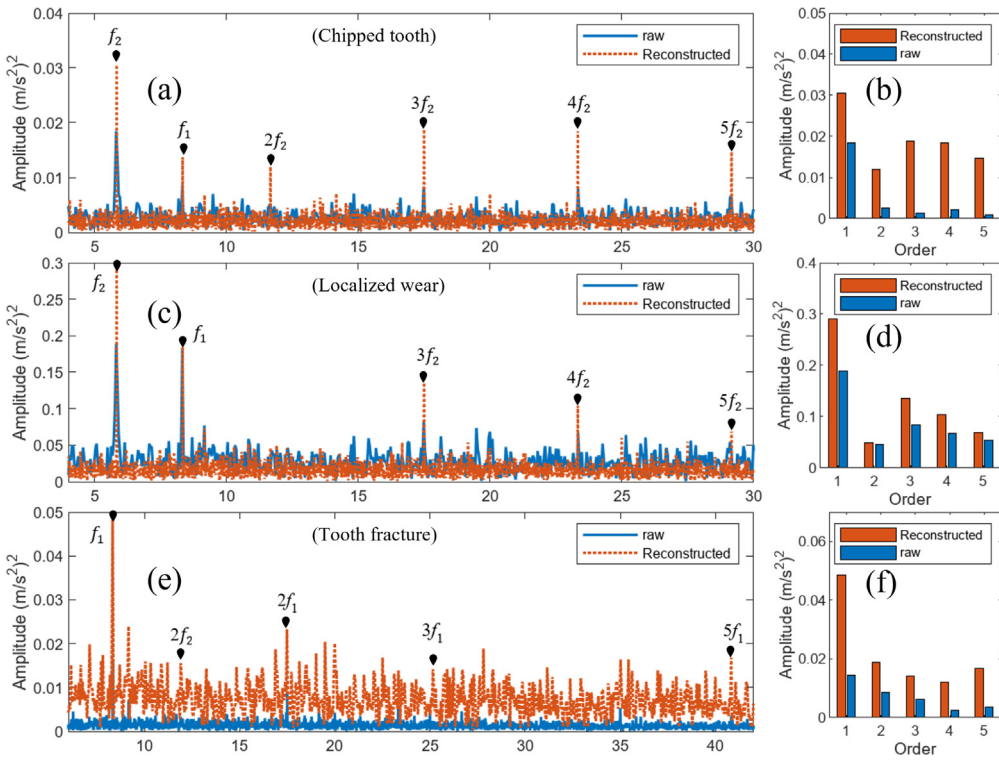


Fig. 20. For FRF $H_{c,pp}$ at 500 r/min, square envelope spectra of different faults and characteristic order spectra of their frequencies : (a),(b) Chipped tooth; (c),(d) Localized wear; (e),(f) Tooth fracture.

$$\begin{vmatrix} a_{11} + \alpha - \lambda_i & a_{12} & \dots & a_{1n} \\ a_{21} & a_{22} + \alpha - \lambda_i & \dots & a_{2n} \\ \vdots & \vdots & \ddots & \vdots \\ a_{n1} & a_{n2} & \dots & a_{nn} + \alpha - \lambda_i \end{vmatrix} = 0$$

$$\begin{vmatrix} a_{11} - (\lambda_i - \alpha) & a_{12} & \dots & a_{1n} \\ a_{21} & a_{22} - (\lambda_i - \alpha) & \dots & a_{2n} \\ \vdots & \vdots & \ddots & \vdots \\ a_{n1} & a_{n2} & \dots & a_{nn} - (\lambda_i - \alpha) \end{vmatrix} = 0 \quad (\text{B.1})$$

$$\begin{vmatrix} a_{11} - \lambda'_i & a_{12} & \dots & a_{1n} \\ a_{21} & a_{22} - \lambda'_i & \dots & a_{2n} \\ \vdots & \vdots & \ddots & \vdots \\ a_{n1} & a_{n2} & \dots & a_{mn} - \lambda'_i \end{vmatrix} = 0 \quad (\text{B.2})$$

By comparison formula (B.1) with formula (B.2), we get the following formula:

$$\lambda_i - \alpha = \lambda'_i \Rightarrow \lambda_i = \lambda'_i + \alpha \quad (\text{B.3})$$

Because α is greater than 0 and A is a positive definite symmetric matrix, $A + \alpha E$ is a positive definite symmetric matrix too. The relation between matrix A , maximum eigenvalue λ_{\max} , and minimum eigenvalue λ_{\min} meet the following constriction:

$$\text{cond}(A) = \frac{\lambda_{\max}(A)}{\lambda_{\min}(A)} \quad (\text{B.4})$$

According to formula (3) and (4), then

$$\text{cond}(A + \alpha E) = \frac{\lambda_{\max} + \alpha}{\lambda_{\min} + \alpha}$$

$$\begin{aligned} \text{cond}(A + \alpha E) - \text{cond}(A) &= \frac{\lambda_{\max} + \alpha}{\lambda_{\min} + \alpha} - \frac{\lambda_{\max}}{\lambda_{\min}} \\ &= \frac{(\lambda_{\max} + \alpha)\lambda_{\min} - \lambda_{\max}(\lambda_{\min} + \alpha)}{(\lambda_{\min} + \alpha)\lambda_{\min}} = \frac{\alpha\lambda_{\min} - \alpha\lambda_{\max}}{(\lambda_{\min} + \alpha)\lambda_{\min}} = \frac{\alpha(\lambda_{\min} - \lambda_{\max})}{(\lambda_{\min} + \alpha)\lambda_{\min}} \end{aligned}$$

So, $\text{cond}(A + \alpha E) < \text{cond}(A)$.

Data availability

The data will be made available on request.

References

- [1] W. Cheng, D. Blamaud, Y. Chu, L. Meng, J. Lu, W.A. Basit, Transfer path analysis and contribution evaluation using SVD-and PCA-based operational transfer path analysis, *Shock Vib.* 2020 (2020).
- [2] Y. Huang, B. Huang, Y. Cao, X. Zhan, Q. Huang, J. Wang, Noise source diagnosis method based on transfer path analysis and neural network, *Appl. Sci.* 13 (22) (2023) 12244.
- [3] W. Yan, S. Zhong, H. Li, J. Chen, J. Yang, Turbo generator vibration source identification based on operational transfer path analysis technology, *J. Vibroeng.* 25 (7) (2023) 1243–1256.
- [4] H. Xue, G. Previati, M. Gobbi, G. Mastinu, Research and development on noise, vibration, and harshness of road vehicles using driving simulators—a review, *SAE Int. J. Veh. Dyn. Stab. NVH* 7 (4) (2023) 555–577.
- [5] F.X. de Melo, L.P.R. de Oliveira, Combining classical and component-based TPA for equivalent load identification, *J. Braz. Soc. Mech. Eng.* 42 (2020) 1–11.
- [6] V.L. Wilke, M.G. Conzemius, M.F. Besancon, R.B. Evans, M. Ritter, Comparison of tibial plateau angle between clinically normal greyhounds and labrador retrievers with and without rupture of the cranial cruciate ligament, *J. Am. Vet. Med. Assoc.* 221 (10) (2002) 1426–1429.
- [7] Z. Wang, P. Zhu, A system response prediction approach based on global transmissibilities and its relation with transfer path analysis methods, *Appl. Acoust.* 123 (2017) 29–46.
- [8] P. Gajdatsy, K. Janssens, L. Gielen, P. Mas, H. Van Der Auweraer, Critical assessment of operational path analysis: effect of coupling between path inputs, *J. Acoust. Soc. Am.* 123 (5) (2008) 3876.
- [9] P. Gajdatsy, K. Janssens, W. Desmet, H. Van Der Auweraer, Application of the transmissibility concept in transfer path analysis, *Mech. Syst. Signal Process.* 24 (7) (2010) 1963–1976.
- [10] D. de Clerk, A. Ossipov, Operational transfer path analysis: theory, guidelines and tire noise application, *Mech. Syst. Signal Process.* 24 (7) (2010) 1950–1962.

- [11] K. Janssens, P. Gajdatsy, L. Gielen, P. Mas, L. Britte, W. Desmet, H. Van der Auweraer, OPAX: A new transfer path analysis method based on parametric load models, *Mech. Syst. Signal Process.* 25 (4) (2011) 1321–1338.
- [12] S. Prenant, T. Padois, V. Rolland, M. Etchessahar, T. Dupont, O. Doutres, Effects of mobility matrices completeness on component-based transfer path analysis methods with and without substructuring applied to aircraft-like components, *J. Sound Vib.* 547 (2023) 117541.
- [13] J. Meggitt, A. Elliott, A. Moorhouse, A. Jalibert, G. Franks, Component replacement TPA: A transmissibility-based structural modification method for in-situ transfer path analysis, *J. Sound Vib.* 499 (2021) 115991.
- [14] O. Guasch, C. García, J. Jové, P. Artís, Experimental validation of the direct transmissibility approach to classical transfer path analysis on a mechanical setup, *Mech. Syst. Signal Process.* 37 (1–2) (2013) 353–369.
- [15] Z. Wang, P. Zhu, J. Zhao, Response prediction techniques and case studies of a path blocking system based on global transmissibility direct transmissibility method, *J. Sound Vib.* 388 (2017) 363–388.
- [16] M.V. van der Seijs, D. De Klerk, D.J. Rixen, General framework for transfer path analysis: History, theory and classification of techniques, *Mech. Syst. Signal Process.* 68 (2016) 217–244.
- [17] Z. Wang, L. Cheng, S. Lei, Y. Yang, L. Ding, An in-situ decoupling method for discrete mechanical systems with rigid and resilient coupling links, *Appl. Acoust.* 195 (2022) 108853.
- [18] J. Brunetti, W. D'Ambrogio, A. Fregolent, Dynamic coupling of substructures with sliding friction interfaces, *Mech. Syst. Signal Process.* 141 (2020) 106731.
- [19] J. Meggitt, A. Moorhouse, In-situ sub-structure decoupling of resiliently coupled assemblies, *Mech. Syst. Signal Process.* 117 (2019) 723–737.
- [20] X. Liao, S. Li, L. Liao, H. Meng, Virtual decoupling method: a novel method to obtain the FRFs of subsystems, *Arch. Appl. Mech.* 87 (2017) 1453–1463.
- [21] X. Li, K. Liu, J. Yang, Study of the rock crack propagation induced by blasting with a decoupled charge under high in situ stress, *Adv. Civ. Eng.* 2020 (2020) 1–18.
- [22] T. Kalaycıoğlu, H.N. Özgüven, Nonlinear structural modification and nonlinear coupling, *Mech. Syst. Signal Process.* 46 (2) (2014) 289–306.
- [23] A. Fregolent, et al., Substructure decoupling without using rotational dofs: fact or fiction, *Mech. Syst. Signal Process.* 72 (2016) 499–512.
- [24] W. D'Ambrogio, A. Fregolent, Replacement of unobservable coupling DoFs in substructure decoupling, *Mech. Syst. Signal Process.* 95 (2017) 380–396.
- [25] T. Duan, J. Wei, A. Zhang, Z. Xu, T.C. Lim, Transmission error investigation of gearbox using rigid-flexible coupling dynamic model: Theoretical analysis and experiments, *Mech. Mach. Theory* 157 (2021) 104213.
- [26] R. Lu, M.R. Shahriar, P. Borghesani, R.B. Randall, Z. Peng, Removal of transfer function effects from transmission error measurements using cepstrum-based operational modal analysis, *Mech. Syst. Signal Process.* 165 (2022) 108324.
- [27] D. Peng, W.A. Smith, P. Borghesani, R.B. Randall, Z. Peng, Comprehensive planet gear diagnostics: Use of transmission error and mesh phasing to distinguish localised fault types and identify faulty gears, *Mech. Syst. Signal Process.* 127 (2019) 531–550.
- [28] L. Keersmaekers, L. Mertens, R. Penne, P. Guillaume, G. Steenackers, Decoupling of mechanical systems based on in-situ frequency response functions: The link-preserving, decoupling method, *Mech. Syst. Signal Process.* 58 (2015) 340–354.
- [29] Z. Wang, P. Zhu, Z. Liu, Relationships between the decoupled and coupled transfer functions: Theoretical studies and experimental validation, *Mech. Syst. Signal Process.* 98 (2018) 936–950.
- [30] Y. Huangfu, X. Dong, X. Yu, K. Chen, Z. Li, Z. Peng, Fault tracing of gear systems: An in-situ measurement-based transfer path analysis method, *J. Sound Vib.* 553 (2023) 117610.
- [31] L. Keersmaekers, L. Mertens, R. Penne, G. Steenackers, P. Guillaume, Decoupling of mechanical systems: the link-preserving, decoupling method, in: Proceedings of ISMA 2014-International Conference on Noise and Vibration Engineering and USD 2014-International Conference on Uncertainty in Structural Dynamics, 2014, pp. 3869–3878.
- [32] N. Roozen, Q. Leclerc, On the use of artificial excitation in operational transfer path analysis, *Appl. Acoust.* 74 (10) (2013) 1167–1174.
- [33] A. Thite, D. Thompson, The quantification of structure-borne transmission paths by inverse methods. Part 2: Use of regularization techniques, *J. Sound Vib.* 264 (2) (2003) 433–451.
- [34] X. Yu, Y. Huangfu, Q. He, Y. Yang, M. Du, Z. Peng, Gearbox fault diagnosis under nonstationary condition using nonlinear chirp components extracted from bearing force, *Mech. Syst. Signal Process.* 180 (2022) 109440.
- [35] X. Yu, C. Cheng, Y. Yang, M. Du, Q. He, Z. Peng, Maximumly weighted iteration for solving inverse problems in dynamics, *Int. J. Mech. Sci.* 247 (2023) 108169.
- [36] D. Lee, T.-S. Ahn, H.-S. Kim, A metric on the similarity between two frequency response functions, *J. Sound Vib.* 436 (2018) 32–45.